The ISOLTRAP Laser-Ablation Ion Source and Q-Value Determination of the ^{110}Pd Double Beta Decay

Diplomarbeit von

Daniel Fink

Institut für Physik
Johannes Gutenberg-Universität Mainz

CERN

The ISOLTRAP Laser-Ablation Ion Source and Q-Value Determination of the ^{110}Pd Double Beta Decay

21. Juni 2010

Contents

List of Figures

List of Tables

1 Introduction

One of the most mysterious and least understood particles in subatomic physics is the neutrino. Produced in nuclear reactions, as for instance in stars like our sun, they usually travel close to speed of light, are electrically neutral, and interact extremely weekly with matter. About 100 billion solar neutrinos flush a human fingernail every second, but the interaction is so weak that in seventy years only a single atom of the human body will have reacted with a neutrino [Dav03].
Postulated by Wolfgang Pauli already in 1933 [Pau77], the neutrinos were believed to be massless for many years. But the physics of neutrinos went through a revolution in the past twenty years. The discovery of the neutrino oscillations by the Sudbury Neutrino Observatory [Ahm02], where the neutrinos change their flavor eigenstates (ν_e, ν_μ, and ν_τ) over long distance and time, led to the first evidence for a non-zero mass, because a mass difference between two neutrino eigenstates is necessary for its explanation. Furthermore, there are strong reasons to assume that neutrinos are their own antiparticles ($\nu_e = \overline{\nu}_e$), in other words they are so-called Majorana particles.
A very promising way to address this issue is the search for the neutrinoless double beta decay ($0\nu\beta\beta$-decay) because it requires massive Majorana neutrinos to occur. Here, an atomic nucleus X decays into the daughter nucleus Y only by emission of two electrons, whereas the emitted neutrino is reabsorbed as an antineutrino. This process violates the total leptonic number conservation by two units and hence, is forbidden with respect to the Standard Model in contrast to its counterpart, the neutrino accompanied double beta decay ($2\nu\beta\beta$-decay), where two electrons and two neutrinos are emitted.
While the $2\nu\beta\beta$-decay could already be observed for several isotopes, such as ^{82}Se, [Ell87], the $0\nu\beta\beta$-decay is still waiting for its proof of existence. However, the predicted half-lives of the $0\nu\beta\beta$-decay are of the order of 10^{26} years, which would make the neutrinoless double beta decay by far the rarest nuclear decay, and its discovery a great challenge for the experimentalists.
The expected signal of the $0\nu\beta\beta$-decay consists of two electrons, which add up to a sharp energy peak in the $\beta\beta$-decay spectrum at the Q-value of the transition. In general, the Q-value is defined as the difference of the energies of the reactants and the products of a reaction or equivalent in the case of nuclear decays as the difference in mass of the mother nucleus and daughter nucleus. Since the peak would rise hardly above the background due to the very few events in time, the Q-value must be determined with an uncertainty below 1 keV to distinguish and identify the peak. In addition, the Q value is a very important parameter to calculate the matrix element M and the phase space G of the transition. In total, the half-life of a ($0\nu\beta\beta$)-decay scales with Q^5. Hence, a high Q-value of a possible double beta decay candidate is advantageous for experiments. Furthermore, the double beta decay is competing with the single beta decay. Only when

the single beta decay is energetically forbidden, the double beta decay can occur.
In total, eleven mass doublets, which fulfill the conditions for $(0\nu\beta\beta)$-decay with a high Q-value of more than 2000 keV were found and are of strong interest for further studies. Tab. 1.1 shows the eleven candidates. Up to now, precise Q-value measurements with uncertainties of less than 1 keV were performed for several double beta decay candidates, namely ^{76}Ge [Dou01, Rah08], ^{100}Mo [Rah08], ^{112}Sn [Rah09], ^{130}Te [Red09], and ^{136}Xe [Red07].

Table 1.1: The eleven $0\nu\beta\beta$-candidates with $Q > 2000$ keV. [Zub04]

Transition	Q**-value (keV)**	**nat. ab.(%)**
$^{48}_{20}\mathrm{Ca}\rightarrow^{48}_{22}\mathrm{Ti}$	4271	0.19
$^{76}_{32}\mathrm{Ge}\rightarrow^{76}_{34}\mathrm{Se}$	2039	7.8
$^{82}_{34}\mathrm{Se}\rightarrow^{82}_{36}\mathrm{Kr}$	2995	9.2
$^{96}_{40}\mathrm{Zr}\rightarrow^{96}_{42}\mathrm{Mo}$	3350	2.8
$^{100}_{42}\mathrm{Mo}\rightarrow^{100}_{44}\mathrm{Ru}$	3034	9.6
$^{110}_{46}\mathrm{Pd}\rightarrow^{110}_{48}\mathrm{Cd}$	2013	11.8
$^{116}_{48}\mathrm{Ca}\rightarrow^{116}_{50}\mathrm{Sn}$	2802	7.5
$^{124}_{50}\mathrm{Sn}\rightarrow^{124}_{52}\mathrm{Te}$	2288	5.64
$^{130}_{52}\mathrm{Te}\rightarrow^{130}_{54}\mathrm{Xe}$	2533	34.5
$^{136}_{54}\mathrm{Xe}\rightarrow^{136}_{56}\mathrm{Ba}$	2479	8.9
$^{150}_{60}\mathrm{Nd}\rightarrow^{150}_{62}\mathrm{Sm}$	3367	5.6

This work reports on the high precise Q-value measurement of the ^{110}Pd double beta decay, which has the highest uncertainty of all eleven candidates in literature [Aud03]. Before the mass doublet was studied in this work, the uncertainty of the literature value of the Q-value is more than 9 keV and the goal within this thesis was to reduce the uncertainty by an order of magnitude to below 1 keV.
A first study on this specific transition goes back to 1951 [Win52]. Here, a direct observation of the neutrinoless double beta decay was attempted, but due to the imprecise Q-value and inaccuracy of the experimental setup, the peak could not be observed. However, a high-precision Q-value is extremely important for future experiments and is thus the motivation of the present study.
The measurements presented in this thesis were performed at the double Penning-trap mass spectrometer ISOLTRAP [Muk08], which is located at the on-line isotope mass separator ISOLDE/CERN [Kug00] in Geneva. In Penning trap experiments, the mass or the Q-value is obtained from the cyclotron frequency $\nu_c = qB/(2\pi m)$, which depends on the mass, charge, and magnetic field. The $^{110}Pd^+$ and $^{110}Cd^+$ ions were produced by the ISOLTRAP laser ablation ion source [Bla02], whose modification and improvement was a major part of this thesis. Here, a new laser was installed as well as new laser optics and several new elements ion optics elements were designed and added to the setup. The cyclotron frequency of the mother nucleus ^{110}Pd and that of of the daughter nucleus ^{110}Cd were measured more than 100 times alternately with a relative uncertainty

of each measurement of about $5 \cdot 10^{-9}$. Their frequency ratio was used to derive the Q-value of the ^{110}Pd/^{110}Cd mass doublet. In addition, mass measurements of ^{110}Pd and ^{110}Cd were performed using for the first time carbon clusters as reference.
The outline of the thesis is the following. In the chapter 2, an overview of the physics of the neutrinoless double beta decay is given. Beginning with a summary of the most important steps in neutrino physics history, the theory of massive Majorana neutrinos is motivated, which is followed by an introduction to double beta decay experiments, where the Q-value and its outmost importance for these experiments is pointed out. In chapter 3 the physics of the Penning trap technique and the experimental setup of ISOLTRAP is discussed in detail. Next, the laser ablation source is described in chapter 4. First, an introduction to laser ablation and its basic principles is given, which is followed by an extensive description and characterization of the setup and its recent modifications. Then, the ion production and preparation process of palladium, cadmium, and carbon cluster ions is given in great detail. In chapter 5, we give a description of two analysis methods, used to determine masses and Q-values with Penning traps and the whole evaluation process including a discussion of all uncertainties and their contribution to the total uncertainty. This chapter closes with the final results obtained within this work on the Q-value and the mass measurements of the ^{110}Pd/^{110}Cd mass doublet and their discussion.

2 Neutrino Physics and Double Beta Decay

Neutrinos were postulated and discovered already in the middle of the last century. Nevertheless, a lot of fundamental, unanswered questions connected to the neutrino's properties are still remaining. Answering those would yield a deeper understanding in particle physics, cosmology, and even in physics beyond the Standard Model. Neutrinos were believed to be massless for a long time. But things changed, when recent experiments showed neutrino oscillations and hence gave the evidence of non-zero masses. However, the absolute masses and the mass hierarchy of the different neutrino flavors are still unknown. Furthermore, the question whether neutrinos are Majorana or Dirac particles is still open, i.e. whether or not they are their own antiparticles ($\nu_e = \overline{\nu}_e$). The neutrinoless double beta decay ($0\nu\beta\beta$) plays a key role in the quest to answer these questions. An important parameter in its proof of existence is the Q-value, which is the difference in energy of the reactants and the products of the transition ($Q = E_{reactants} - E_{products}$). In the following, an introduction to neutrino and double-beta-decay physics is given.

2.1 Neutrino Physics

2.1.1 Milestones in Neutrino physics

In 1930, Wolfgang Pauli postulated the neutrinos for the very first time in order to save the law of conservation of energy in the β-decay spectrum, which could not 'be explained within a two-body-model [Pau77]. The latter would lead to a sharp peak at the Q-value of the transition, but instead, the spectrum of a beta decay shows a continuous energy distribution as shown in fig. 2.1 a). Pauli predicted the neutrino to be massless or at least very light, to be neutral to the electromagnetic force and to have spin 1/2, i.e., to be a fermion. However, it took more than 20 years until the group of Clyde L. Cowan and Frederick Reines detected the electron neutrino ν_e (or rather the antineutrino $\overline{\nu_e}$) by observing an inverse beta decay in 1956 for the first time [Rei56]:

$$\overline{\nu}_e \quad + \quad p \quad \rightarrow \quad e^+ \quad + \quad n\,. \tag{2.1}$$

Later, the muon neutrino (ν_μ) and tau neutrino (ν_τ) were discovered in 1962 [Dan62] and 2000 [Kod01], respectively. At present, the three neutrinos are considered neutral and are fully integrated into the very successful Standard Model of particle physics. Unlike other leptons, up to now, only left-handed neutrinos (helicity = -1) and right-handed antineutrinos (helicity = +1) were observed in weak interactions. Fig. 2.1 b) shows a Feynman diagram of the neutron beta decay, how it is described in the Standard Model. Contrary to the Standard Model, recent experiments have shown that the neutrinos

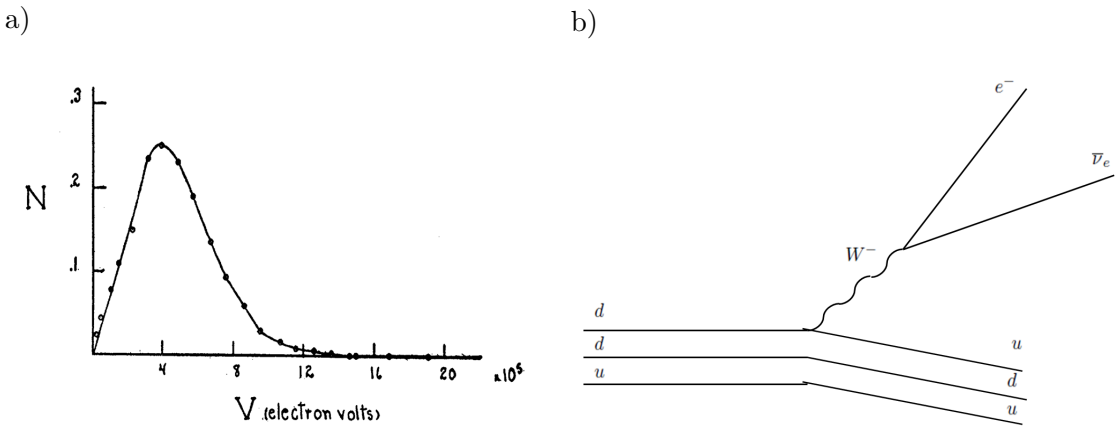

Figure 2.1: a) Beta spectrum of radium as measured by F.A. Scott in 1935. [Sco35]. b) Feynman diagram of the neutron beta decay.

undergo oscillations, i.e. they change their flavor eigenstates in time, which is already known to be the case from quarks. First evidence was given by the Homestake experiment (running continuously from 1970 to 1995), where Raymond Davis Jr. and his team observed the electron neutrinos from the sun in the reaction [Dav94]

$$\nu_{\mathrm{e}} \quad + \quad {}^{37}\mathrm{Cl} \quad \rightarrow \quad {}^{37}\mathrm{Ar} \quad + \quad \mathrm{e}^- \,. \tag{2.2}$$

On average, about one neutrino per two days was detected, which is half as much as one would expect from the Standard Solar Model. This was the origin of the so-called solar neutrino problem. Later experiments such as KAMIOKANDE (KAMioka Experiment, 1986-1995) [Hir90], GALLEX (GALlium EXperiment,1991-1996) [Ans95], Superkamiokande (Super KAMioka Experiment, 1996-2001) [Col02] and GNO (Gallium Neutrino Observatory, 1998 - 2003) [Col00] confirmed the missing amount of neutrinos. The missing solar neutrinos can be explained by neutrino oscillations, which allow the neutrinos to change their flavor while traveling from the source to the detector. Finally, the Sudbury Neutrino Observatory SNO (in operation since 1999) cleared the last doubts about the neutrino oscillations [Ahm02]. SNO could detect all three neutrino flavors at the same time and showed that the overall measured amount of neutrinos is consistent with the latest solar models. The effect of neutrino oscillation has a major impact on the neutrino physics, since it provides evidence of a non-zero neutrino mass. In addition, it caused the concept of conservation of the leptonic family number to be given up. However, the neutrino oscillations give access only to $\Delta m^2_{i,j} = m^2_i - m^2_j$ between two mass eigenstates with $i, j = 1, 2, 3$. The latest results from solar neutrino experiments and similar experiments with neutrinos from nuclear power plants lead to $\Delta m^2_{1,2} = 7.1^{1.2}_{-0.6} \cdot 10^{-5}\,\mathrm{eV}^2$ [Ahm04]. Presently, experiments focus on determining the exact masses of the three neutrino eigenstates. For this purpose experiments search for a small deviation near the endpoint of the β-decay spectrum. The Mainz-Troitsk

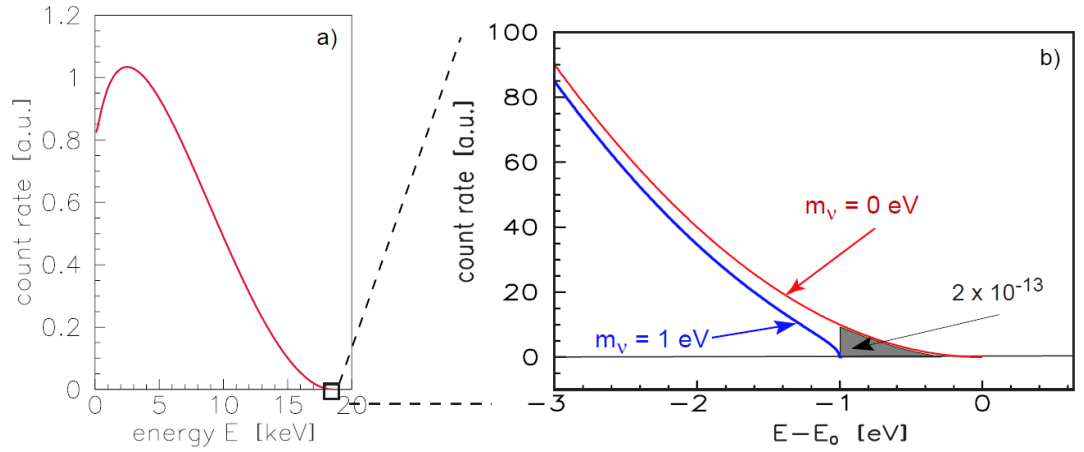

Figure 2.2: Basic idea of the measurement principle of the Mainz-Troitsk experiment and KATRIN experiment. The experiments search for a small deviation near the endpoint in the β-decay spectrum. [KAT05].

experiment [Ott08] lowered the upper mass limit of ν_e to 2 eV. Fig. 2.2 illustrates the basic idea. Among these, the KATRIN experiment (KArlsruhe TRItium Neutrino experiment) wants to improve this limit by one order of magnitude by studying the tritium β-decay endpoint. Another promising approach is to detect a neutrinoless double beta decay ($0\nu\beta\beta$). This decay mode can provide an absolute value of the neutrino mass and would give evidence that neutrinos are massive Majorana particles (i.e. they are their own antiparticles). In spite of several experiments studying this topic, there is still no unambiguous result. In this respect, the Heidelberg-Moscow experiment [Gue97] should be pointed out, where one part of the collaboration claims to have detected a $0\nu\beta\beta$-decay signal of ^{76}Ge, which is not confirmed by the other part of the collaboration. Upcoming experiments will hopefully bring a definite answer.

2.1.2 Physics of Massive Neutrinos

The neutrinos are included into the minimal Standard Model of the electroweak interaction by Glashow, Weinberg and Salam as massless fermions [Gla80, Wei80, Sal80]. Their model characterizes the neutrinos as follows:

1. Only V-A interaction takes place in weak interactions. The gauge group is $SU(2)_L \times U(1)$.
2. No right-handed neutrinos and no left-handed antineutrinos exist. This means that there is no Dirac mass term for neutrinos.
3. Only charged fermions and gauge bosons have mass, which means that no mass (and especially no Majorana mass) exists for neutrinos.
4. Only the flavor mixing of the quarks is a source for CP violation.

The assumptions mentioned above are for the most part only based on experimental results. The V+A interaction might exist, but was never observed in any weak interaction similar to the fact that neutrino masses were never measured directly. For instance, lepton number conservation is a consequence of that model, but no Noether symmetry was yet found, which could give this conservation law a deeper theoretical fundament. On the other hand, neutrino oscillation experiments provide evidence for finite neutrino masses. Hence, there is space for modifications and new neutrino physics could open the door for physics beyond the Standard Model. Especially the following questions are of main interest:

1. What are the exact values of the neutrino mass eigenstates ν_i(i=1,2,3)? In which mass hierarchy are they arranged?

2. Why are neutrinos obviously so much lighter than electrons?

3. Are neutrinos of Dirac or Majorana mass type?

4. Why do only left-handed charged currents occur in the weak interaction? Do right-handed currents exist, too?

Weyl, Dirac and Majorana Neutrinos

There exists several neutrino models. In case of massless neutrinos, the Weyl representation of the wavefunctions is sufficient. In case of massive neutrinos, a Dirac representation or a Majorana representation, depending on the mass type, is necessary. The following part gives an overview of the different theoretical models. The theory is described in greater detail in [Doi85] and [Zub98].
The wave functions of fermions have to fulfill the Dirac equation:

$$(i\gamma_\mu \partial^\mu - m)\,\Psi\,(x) = 0\,. \tag{2.3}$$

In general, the solution consists of four linearly independent basis vectors: Ψ_R, Ψ_L, $\overline{\Psi}_R$ and $\overline{\Psi}_L$. In case of massless neutrinos, i.e. in the Standard Model, the Weyl representation describes the massless spin 1/2 particles correctly with respect to the helicity. The Weyl spinors are 2-component spinors, which are the left and right handed projection of a 4-component spinor Ψ[1]:

$$\Psi_{L,R} = \frac{1}{2}\,(1 \pm \gamma_5)\,\Psi\,. \tag{2.4}$$

Hence, the Dirac equation decouples into two independent equations. Since neutrinos don't carry electrical charge, an alternative description as Majorana neutrinos is possible.

[1]Here, the gamma matrices γ^μ are given in the Weyl basis by: $\gamma^0 = \begin{pmatrix} 0 & 1 \\ 1 & 0 \end{pmatrix}$, $\gamma^i = \begin{pmatrix} 0 & \sigma^i \\ -\sigma^i & 0 \end{pmatrix}$, and $\gamma^5 = \begin{pmatrix} -1 & 0 \\ 0 & 1 \end{pmatrix}$, where σ^i are the Pauli matrices and $i = 1, 2, 3$.

Majorana fermions are their own antiparticles (charge conjugates) $\nu_\alpha = \overline{\nu_\alpha}$, which can be represented using the charge conjugation operator:

$$C^{-1}\gamma_\mu C = -\gamma_\mu^T \ . \tag{2.5}$$

Now, two neutrino fields can be constructed,

$$\nu_1 = \frac{\Psi_L + (\Psi_R)^C}{\sqrt{2}} \quad \text{and} \quad \nu_2 = \frac{\Psi_R + (\Psi_L)^C}{\sqrt{2}} \,, \tag{2.6}$$

since $(\Psi_R)^C$ is left-handed and $(\Psi_L)^C$ is right-handed. It was shown, that the Majorana description is equivalent to the Weyl description for massless neutrinos, if the neutrinos only interact by the V-A interaction. Nevertheless, for massive neutrinos, the Weyl description is not sufficient any more and instead a four component spinor is necessary. In the case of Dirac masses, Ψ_R and $\overline{\Psi_L}$ are treated as sterile with respect to the weak interaction as they do not couple to the gauge boson. However, the question whether neutrinos are Majorana or Dirac particles remains still unanswered. More general is a combination of both, Majorana and Dirac masses. Then the mass term of the lagrangian density for N neutrino flavors is given by:

$$\mathcal{L}_m = \begin{pmatrix} \overline{\Psi_L} & \overline{\Psi^C}_L \end{pmatrix} \underbrace{\begin{pmatrix} m_L^M & m^D \\ m^D & m_R^M \end{pmatrix}}_{\mathcal{M}_{2N\times 2N}} \begin{pmatrix} \Psi_R^C \\ \Psi_R \end{pmatrix} \ + \ h.c. \,, \tag{2.7}$$

where m_L^M, m_R^M, m^D represent the mass coupling parameters of the Majorana and Dirac mass fields and $h.c$ is the complex conjugate of the first part of the equation. The eigenvalues of the mass matrix $\mathcal{M}_{2N\times 2N}$ give the physical masses. Therefore, it is very instructive to study the case of only one neutrino generation. The two eigenvalues are given then by diagonalizing $\mathcal{M}_{\in\times\in}$:

$$\begin{pmatrix} m_L^M & m^D \\ m^D & m_R^M \end{pmatrix}_{N=1} \quad \Longrightarrow \quad m_{1,2} = \frac{1}{2}\left(m_L^M + m_R^M\right) \pm \frac{1}{2}\sqrt{\left(m_L^M - m_R^M\right)^2 + \left(2m^D\right)^2} \,. \tag{2.8}$$

The final mass ratio of m_L^M, m_R^M and m^D determines the physics of the neutrinos. For instance, if $m_L^M = m_R^M = 0$, the neutrino is a pure Dirac neutrino with a degenerated mass $m_{1,2} = m^D$, whereas $m^D = 0$ and $m_{1,2} = m_L^M, m_R^M$ ends up in the other extreme, a pure Majorana neutrino with two mass eigenstates. Several mixtures with differently weighted m^D and $m_{L,R}^M$ are possible, in which the "see-saw" mechanism has to be pointed out. This mechanism was developed by Gell-Mann, Ramond and Slansky and by Yanagida in 1979. The advantage of that model is that it can explain very nicely the small neutrino masses. The basic idea is to assign the left- and right-handed Majorana masses different values and to leave the Dirac mass of the same order as that of other charged leptons and quarks. This seems to be more natural than an artificial small Dirac mass separately constructed for neutrinos in contrast to other leptons and quark masses.

Additionally, the see-saw mechanism, as well as Majorana masses are therefore preferred in the grand unified theories (GUT). The mass hierarchy in the "see-saw-mechanism" is given by:

$$m_M^M L << m^D << m_R^M \,. \tag{2.9}$$

This leads, for example with $m_L^M = 0$, to the eigenvalues

$$m_1 = \frac{\left(m^D\right)^2}{m_R^M} \tag{2.10}$$

and

$$m_2 = m_R^M \left(1 + \frac{\left(m_D^M\right)^2}{\left(m_R^M\right)^2}\right) \approx m_R^M \,. \tag{2.11}$$

Hence, the neutrino mass is split into a very light and a very heavy neutrino mass. Different models exist and predict masses from $m_1 < 1\,\mathrm{eV}$ to masses of up to $m_2 = 10^{16}$ GeV [Zub98].

Flavor Mixing of Massive Neutrinos

Similar to the quark sector, the weakly interacting flavor eigenstates of the neutrinos don't have necessarily to be necessarily identical with the mass eigenstates. Then both eigenstates can be connected by an unitrary matrix U,

$$\nu_\alpha = \sum_i U_{\alpha i} \nu_1 \quad \text{with} \quad \alpha = \mathrm{e}, \nu, \tau \quad , \tag{2.12}$$

which is called the Pontecorvo-Maki-Nakagawa-Sato (PMNS)-matrix. In case of three interacting Majorana neutrinos, the mixing matrix is given by

$$U = \begin{pmatrix} c_{12} & s_{12}c_{13} & s_{13}e^{-i\delta} \\ -s_{12}c_{23} - c_{12}s_{23}s_{13}e^{i\delta} & c_{12}c_{23} - s_{12}s_{23}s_{13}e^{i\delta} & s_{23}c_{13} \\ s_{12}s_{23} - c_{12}c_{23}s_{13}e^{i\delta} & -c_{12}s_{23} - s_{12}c_{23}s_{13}e^{i\delta} & c_{23}c_{13} \end{pmatrix} \mathrm{diag}\left(1, \quad e^{i\alpha_2}, \quad e^{i\alpha_3}\right) \,, \tag{2.13}$$

where s_{ij} stands for the sine of the mixing angles θ_i and c_{ij} for the cosine. The Dirac phase δ and the Majorana phases α_1 and α_2 are sources for CP-violation. Neutrino oscillations are the best known effects of flavor mixing. The probability to find a neutrino ν_β at a distance x from a ν_α-source in a two-flavor mixing model can be calculated by

$$P\left(\nu_\alpha \to \nu_\beta\right) = \sin^2 2\theta \frac{\pi x}{L} \tag{2.14}$$

with the mixing angle θ and the oscillation length L

$$L = \frac{4\pi E\hbar}{(\underbrace{\mid m_\beta^2 - m_\alpha^2 \mid}_{\Delta m_{\alpha\beta}^2})c^3} = 2.48 \left(\frac{E}{MeV}\right)\left(\frac{eV^2}{\Delta m_{\alpha\beta}}\right) m\,. \tag{2.15}$$

flavor mixing also effects the $0\nu\beta\beta$-decay, since the actual measured quantity is the effective Majorana mass, which is a superposition of the mass eigenstates m_i weighted by the matrix elements of the PMNS-matrix U:

$$\langle m_{\nu_e}\rangle = \left|\sum_i U_{ei}^2 m_i\right| = \left|\sum_i \left|U_{ei}^2\right| e^{2i\alpha_i} m_i\right| \quad i = 1,2,3 \tag{2.16}$$

The neutrinoless double beta decay might be the only way to get access to the two Majorana phases $\alpha_{1,2}$ in the mixing matrix U.

2.2 Double Beta Decay

In its most general form, the double beta decay can be defined as a radioactive decay, in which the atomic charge number Z is changed by 2 units, while the atomic mass number A is conserved. Since the double beta decay is one of the rarest nuclear processes known, it has to fulfill several conditions in order to occur and to be observed. Based on the theory of neutrinos, which was discussed in the previous chapter, different double beta decay channels are possible. Of special interest for this thesis are the two electron emitting modes, namely

- the neutrino accompanied mode, first proposed by Mayer in 1935 [GM35]:

$$(\mathrm{A,Z}) \rightarrow (\mathrm{A,Z\text{-}2}) + 2\mathrm{e}^- + 2\overline{\nu}_e \quad (2\nu\beta\beta) \tag{2.17}$$

- and the neutrinoless mode discussed by Furry in 1939 [Fur39]:

$$(\mathrm{A,Z}) \rightarrow (\mathrm{A,Z\text{-}2}) + 2\mathrm{e}^- \quad (0\nu\beta\beta)\,. \tag{2.18}$$

The outstanding importance of the $0\nu\beta\beta$-decay for the neutrino physics and the key-role of the Q-value in its detection is pointed out in detail below.

2.2.1 Theoretical Basis

Conditions

The $\beta\beta$-decay is a second-order process of the weak interaction and hence very rare with very long half-lives. Furthermore, it competes with the single β-decay along isobaric chains, which means that the β-decay has to be either energetically forbidden or at least strongly suppressed by spin arguments. The situation can be easily illustrated

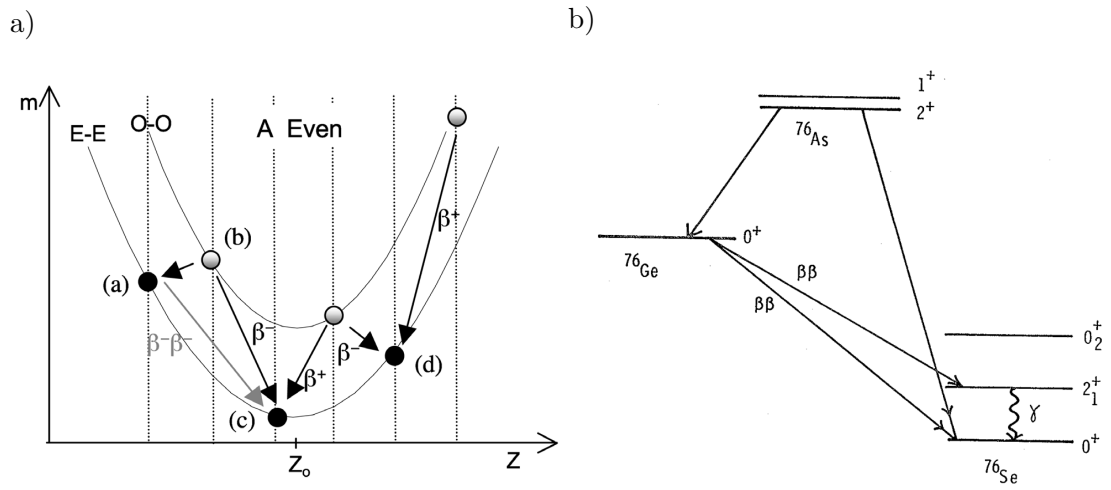

Figure 2.3: a) The two mass parabolas for a specific atomic mass number [Zub04]. The left slope involves electron decays, while the right slope involves positron decays. b) Decay scheme of ^{76}Ge. [Doi85].

by the semi-empirical von Weizsäcker mass formula, based on the liquid drop model [Wei05, Bet36], which leads to mass parabolas for isobars. The binding energy can be approximated with

$$E_B(A,Z) = a_V A - a_S A^{\frac{2}{3}} - a_C \frac{Z(Z-1)}{A^{\frac{1}{3}}} - a_A \frac{(Z-A/2)^2}{A} + \delta(A,Z) \;, \tag{2.19}$$

where a_V is the volume parameter, a_S the surface parameter, a_C the electrostatic repulsion parameter, and a_A the parameter of the asymmetry between the number of protons and neutrons in a nucleus. The last term is the pairing term given by

$$\delta(A,Z) = \begin{cases} +\delta_0 & N,Z \text{ even } (A \text{ even}) \\ 0 & A \text{ odd} \\ -\delta_0 & N,Z \text{ odd } (A \text{ even}) \end{cases} , \tag{2.20}$$

and takes the spin coupling of the nucleons into account[2]. Leaving the mass number A in eq. (2.19) constant leads to a parabola. While there is only one parabola in case of odd A, the binding energy splits into two parabolas for an even A, making the double beta decay possible. Fig. 2.3 a) shows such two mass parabolas. The nuclei decay along the isobaric chain towards the minimum of both parabolas. The decay along the left slope involves electrons and along the right slope positrons. The decay chains switch between the two parabolas and if the next nucleus has a higher mass, the single beta decay is energetically forbidden ($m(Z,A) < m(Z+1)$ or $m(Z,A) < m(Z-1)$ for

[2] A possible parameterization of the parameters is: $a_V = 15.67\,\mathrm{MeV/c^2}$, $a_S = 17.23\,\mathrm{MeV/c^2}$, $a_C = 0.714\,\mathrm{MeV/c^2}$, $a_A = 93.15\,\mathrm{MeV/c^2}$, and $\delta_0 = 11.2\,\mathrm{MeV/c^2}$ [Seg77].

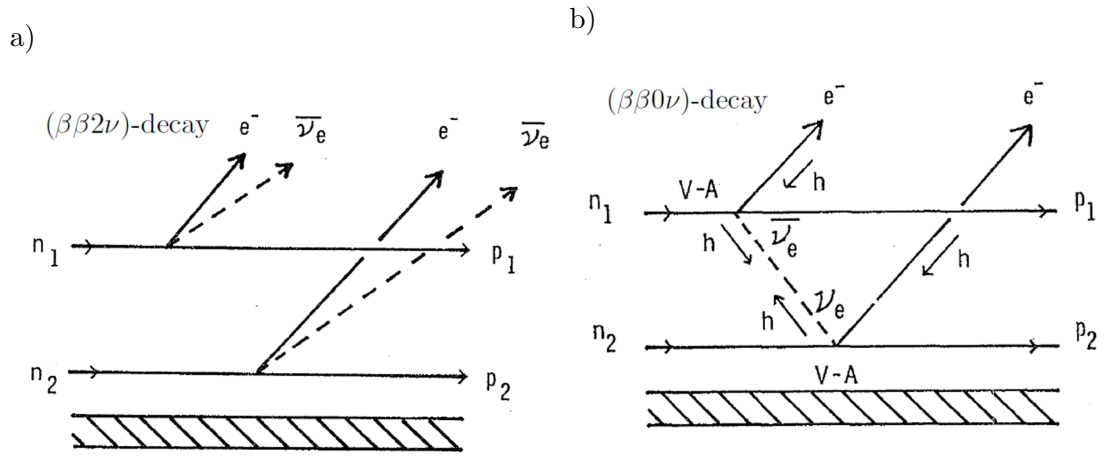

Figure 2.4: a) Diagram of the $\beta\beta 2\nu$-mechanism. b) $\beta\beta 0\nu$ mode with V-A interaction [Doi85].

the β^+-decay). In this case the only way to get closer to the minimum of the isobaric parabola is by two subsequent steps, namely the double beta decay. Fig. 2.3 b) shows the energy level structure of ^{76}Ge. The β-transition from the ^{76}Ge ground state to the energetically higher ^{76}As is not possible. Therefore only double-beta transitions to the ^{76}Se states take place. Since all double beta emitters start from the lower parabola, i.e. they are even-even nuclei, the dominating transitions are all of the form $0^+ \rightarrow 0^+$. In addition, the single β-decay can be also suppressed by high change of the spin as it is for ^{96}Zr $\rightarrow^{96}$ Mo. In total, there are 35 isotopes, which fulfill one of these conditions. Furthermore, the half-life of the $\beta\beta$-decay depends strongly on the size og the Q-value of the transitions, as will be discussed in the following chapters in greater detail. While the rate of the $0\nu\beta\beta$-decay scales with $\propto Q^5$, the rate of $\beta\beta 2\nu$ scales with $\propto Q^{11}$. Hence, in both cases is a higher Q-value hereby a great advantage when trying to observe the $\beta\beta$-decay. In tab. 1.1, the eleven most promising $\beta\beta 0\nu$-candidates with a Q-value higher than 2000 keV are listed. Within this thesis, the Q-value of the ^{110}Pd$\rightarrow^{110}$Cd double beta decay was determined by high-precision Penning trap spectroscopy.

Principles of the Double Beta Decay

The two above mentioned types of double beta decay have different natures. The $2\nu\beta\beta$-decay is in accordance with the conditions of the Standard Model and is only restricted by energy arguments as discussed in the previous chapter. Fig. 2.4 a) shows the simultaneous decay of two neutrons, emitting two electrons e^- and two antineutrinos $\overline{\nu}_e$ at the same time. Assuming the dominating $0^+ \rightarrow 0^+$ transition, the predicted half-life of the $2\nu\beta\beta$-decay is given by [Zub98]

$$\left(T^{2\nu}_{1/2}\right)^{-1} = G^{2\nu}\left(M^{2\nu}_{GT}\right)^2 , \tag{2.21}$$

where $G^{2\nu} \propto Q^{11}$ is the phase space and $M_{GT}^{2\nu}$ the matrix element of the transition.
In contrast to the neutrino emitting double beta decay, the neutrinoless mode is not allowed within the Standard Model, since it violates the total lepton number conservation by two units. The $\beta\beta0\nu$-mode, which Furry discussed first, is shown in fig. 2.4 b). Here, a virtual right-handed antineutrino is emitted at the vertex of n_1. To be absorbed at the vertex of n_2 it has to be a left-handed neutrino. Two conditions have to be fulfilled, to allow that process:

1. The neutrino has to be its own antineutrino ($\nu_e = \overline{\nu_e}$), which means that the neutrino is a Majorana particle.

2. The helicity has a $+1$-component and a -1-component at the same time, which is fulfilled for massive particles.

The assumption that only V-A current appears and light neutrinos ($m_\nu \leq 1\,\mathrm{MeV}$) are involved leads to a half-life of [Zub98]

$$\left(T_{1/2}^{0\nu}\right)^{-1} = G^{0\nu} \left(M^{0\nu}\right)^2 \left(\frac{\langle m_{\nu_e} \rangle}{m_e}\right)^2 , \tag{2.22}$$

where additionally to the phase space and the matrix element, the effective neutrino mass $\langle m_{\nu_e} \rangle$ appears. Besides the fact that a measurement of a $0\nu\beta\beta$-decay would prove the Majorana character, $0\nu\beta\beta$-decay might be the only way to measure the neutrino mass directly due to the restricted sensitivity of direct measurements with the single beta decay for very small neutrino masses. For completeness, it should be mentioned that the model of Furry can be generalized to include also right-handed V+A current. There exist also positron emitting decays. For instance, ^{106}Cd is a possible candidate for double positron decay. In general, the mother nucleus decays by emitting two positrons and two electron neutrinos

$$(Z, A) \rightarrow (Z - 2, A) + 2e^+ + 2\nu_e \,. \tag{2.23}$$

Double positron decay is always accompanied by a single β^+-decay and EC (electron capture) combination

$$e^- + (Z, A) \rightarrow (Z - 2, A) + e^+ + 2\nu_e \tag{2.24}$$

or even double electron capture

$$2e^- + (Z, A) \rightarrow (Z - 2, A) + 2\nu_e \,. \tag{2.25}$$

$\beta^+\beta^+$ and β^+EC are even rarer than the electron emitting ones, since the Q-value is reduced by $4m_ec^2$ in addition to the Coulomb-barrier. Although the half-lives of these processes are as high as 10^{26} years, the detection of a β^+EC decay would give the information whether the $0\nu\beta\beta$-decay is dominated by Majorana masses or by right-handed currents [Hir94].

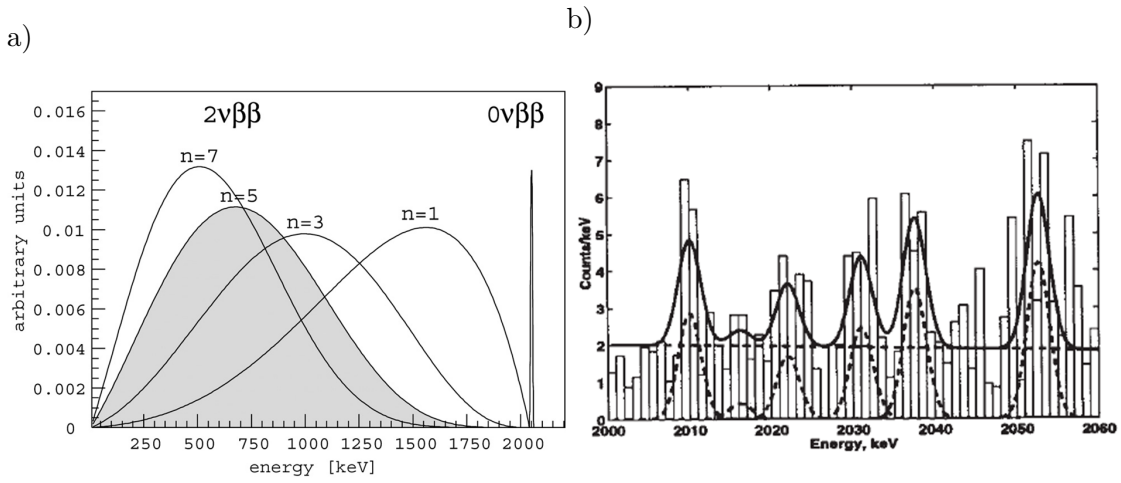

Figure 2.5: a) Scheme of the idealized spectrum of ^{76}Ge. Each event represents the sum energy of the two emitted electrons. [Zub04]. b) Spectrum of ^{76}Ge in the region of the expected $\beta\beta0\nu$-peak, measured by the Heidelberg-Moscow experiment. [KK04]

2.2.2 Double Beta Decay Experiments and Q-values

In general, the $\beta\beta$-experiments can be divided into three groups [Zub04]:

1. Direct counting
2. Geochemical
3. Radiochemical.

Geochemical experiments search for an isotopic anomaly of the daughter nucleus in natural abundances of possible $\beta\beta$-decay candidates, such as ^{82}Se, ^{128}Te and ^{130}Te. The radiochemical experiments use the decay signals of the daughter nuclei of ^{232}Th and ^{238}U. Suitable daughter nuclei are hereby noble gases. Both, the geochemical and the radiochemical methods are limited by the fact that they are only able to measure the total amount of daughter nuclei and cannot distinguish between neutrino accompanied and neutrinoless double decay. Only the direct counting experiments give access to that information. On the other hand, the low event rates of $\beta\beta$-decays make its detection a challenge. Half-lives from around 10^{20} years for $(2\nu\beta\beta)$ up to 10^{26} years for $(0\nu\beta\beta)$ request highest detection sensitivity. Especially, a very low background radiation is necessary. For instance, natural decay chains of U and Th, ^{40}K, Rn, neutrons, and atmospheric particles such as muons have to be excluded or suppressed as much as possible. Nevertheless, even with such an high effort, the background radiation is still in the order of magnitude of the possible double beta decays. The neutrinoless mode is a two body problem ($m_{nuclei} >> m_e$) in contrast to the $2\nu\beta\beta$-decay. While $(2\nu\beta\beta)$

shows a coninuous curve, for the $0\nu\beta\beta$-decay the energy conservation requires a sharp peak at the Q-value of the decay. In general, the Q-value is given by the difference of the energies of the reactants and the products of a reaction:

$$Q = E_{reactants} - E_{products} \,. \tag{2.26}$$

In case of the neutrinoless double beta decay, the Q-value represents only the kinetic energy of the two emitted electrons. Here, the Q-value is equivalent to

$$Q = m_{mother} - E_{daughter} \,. \tag{2.27}$$

An idealized spectrum of ^{76}Ge is shown in fig. 2.5 a). The grey shaded curve represents the sum of the energies of the two emitted electrons in the $2\nu\beta\beta$-decay, while the other curves are more exotic decays, which are not considered within this thesis. The sharp peak at the Q-value of around 2039 keV comes from the $0\nu\beta\beta$-decay. Fig. 2.5 b) shows a spectrum of the Heidelberg-Moscow experiment [KK04] and underlines the importance to know the Q-value as accurate as possible. Hence, if the Q-value is known precisely enough, the peak can be identified in the midst of all the other background peaks. At least six peaks can be identified, whereas only the peak at around 2039 keV should be the $\beta\beta0\nu$ candidate. Therefore, the Q-value between ^{76}Ge and ^{76}Se was measured to 2039.006 keV with an uncertainty of only 50 eV at the SMILETRAP experiment [Dou01]. Future experiments with an higher efficiency and lower background ratio have to prove whether the peak in the Heidelberg-Moscow experiment comes from an $0\nu\beta\beta$-decay or not. Furthermore, precise Q-values are needed to calculate the phase space $G^{2\nu}$ and $G^{0\nu}$ and the matrix elements $M^{2\nu}$ and $M^{0\nu}$ of both the neutrino accompanied and neutrinoless double beta decay. There exists the possibility that for several $\beta^+\beta^+$-decay candidates, the half-life is shortened by several orders of magnitude due to resonances of the ground state of the mother nuclide and excited states of the daughter nuclide and hence, these isotopes become very interesting for future experiments. Here, the Q-values have to be known to an uncertainty down to 200 eV in order to calculate the excited states precisely enough. One of these candidates is the ^{106}Cd$\rightarrow^{106}$Pd transition which can be measured with the Penning trap mass spectrometer ISOLTRAP [Muk08] at ISOLDE/CERN [Kug00]. To this end several modifications to the off-line ion source of ISOLTRAP have been mandatory and performed within the context of this thesis.

3 The ISOLTRAP Setup for High-Precision Mass and Q-Value Measurements

The ISOLTRAP experiment [Muk08] is a tandem Penning trap mass spectrometer at the radioactive ion beam facility ISOLDE at CERN in Geneva, Switzerland [Kug00]. ISOLTRAP allows high-precision mass measurements with a relative uncertainty of $1 \cdot 10^{-8}$ and below. The main goal of ISOLTRAP are mass measurements on exotic, short-lived isotopes, produced and delivered by ISOLDE. Up to now, more than 400 isotopes have been investigated [Kow10]. Within this thesis, the setup has been also used for Q-value measurements with uncertainties below 1 keV. In the following chapter, the principle of Penning trap mass spectrometry and the ISOLTRAP setup will be described in detail.

3.1 The Penning Trap

Penning traps are able to store charged particles in three dimensions using static electric and magnetic fields [Deh90]. In general, the Penning trap consists of a strong homogeneous magnetic field superposed perpendicularly with a weak electrostatic quadrupole field. The magnetic field B forces a charged particle with mass m and charge q on a circular motion with the cyclotron frequency

$$\omega_c = \frac{q}{m} B \,. \tag{3.1}$$

Most common electrode designs are either cylindrically or hyperbolically shaped as shown in fig. 3.1. The first trap of ISOLTRAP, namely the preparation trap, is for practical reasons cylindrical, while the second trap is a hyperbolic Penning trap. What is important is that the geometry approximates the quadrupole field in the center of the trap as well as possible. In the following, the ideal case with infinite electrodes is discussed at first, which generates a pure quadrupole field. Later on, the real Penning trap and its deviations from the ideal case are described.

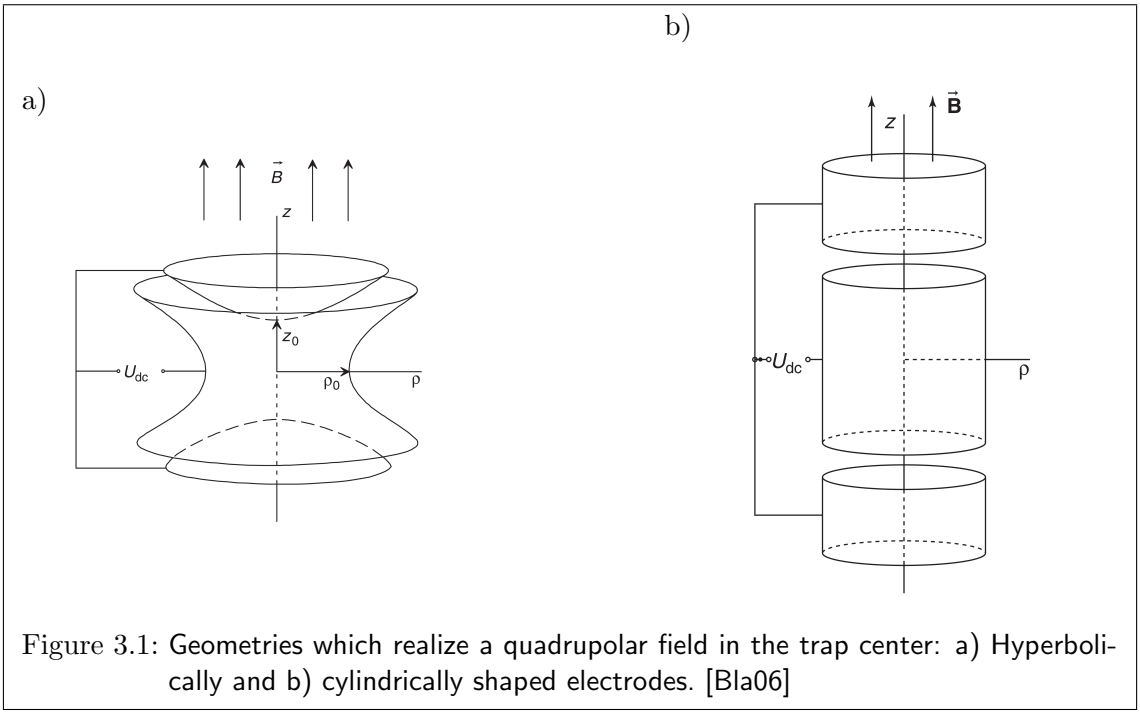

Figure 3.1: Geometries which realize a quadrupolar field in the trap center: a) Hyperbolically and b) cylindrically shaped electrodes. [Bla06]

3.1.1 Principles of an Ideal Penning Trap

Field Geometry of an Ideal Penning Trap

An ideal Penning trap can be characterized by a superposition of a strong homogeneous magnetic field $\vec{B} = B\hat{e}_z$ and an electrostatic quadrupole field ϕ, given by

$$\phi\left(\rho, z\right) = \frac{U_{dc}}{4D^2}\left(2z^2 - \rho^2\right) , \tag{3.2}$$

where $\rho^2 = \left(x^2 + y^2\right)$ is the radius in the x-y-plane, D^2 is a geometrical trap parameter, and U_{dc} is the electrostatic potential applied to the trap electrodes. Fig. 3.1 a) shows a cross section of a hyperbolic Penning trap. Here, the quadrupole potential can be reproduced by placing the electrodes along the equipotential surfaces of $\phi\left(\rho, z\right)$. Therefore, the two endcap electrodes have to fulfill

$$z^2 = z_0^2 + \rho^2/2\,, \tag{3.3}$$

while the ring electrode has to match the condition

$$z^2 = \frac{1}{2}\left(\rho^2 - \rho_0^2\right) . \tag{3.4}$$

Penning traps with finite hyperbolic geometries are able to approximate the quadrupole field in the center of the trap, but field corrections have to be considered additionally.

Equations of Motions

A charged particle inside a Penning trap is confined by the Lorentz force $\vec{F}_L = q\left(\vec{E} + \vec{v} \times \vec{B}\right)$, where the electrostatic field can be calculated using eq. (3.2):

$$\vec{E} = -\vec{\nabla}\phi\left(x, y, z\right) = \frac{U_{dc}}{2d^2}\begin{pmatrix} x \\ y \\ -2z \end{pmatrix} . \tag{3.5}$$

Then, the equations of motion follow from Newton's second law with

$$m\vec{a} = q\left(\vec{E} + \vec{v} \times \vec{B}\right) . \tag{3.6}$$

This leads to the following equations in the radial direction

$$\ddot{x} - \omega_c \dot{y} - \frac{\omega_z^2}{2} x = 0 \,, \tag{3.7}$$

$$\ddot{y} + \omega_c \dot{x} - \frac{\omega_z^2}{2} y = 0 \tag{3.8}$$

and axial direction

$$\ddot{z} + \omega_z^2 z = 0 \,, \tag{3.9}$$

where ω_c is the cyclotron frequency (see eq. (3.1)) and the newly introduced axial frequency ω_z is given by

$$\omega_z = \sqrt{\frac{qU_{dc}}{mD^2}} \,. \tag{3.10}$$

The axial component decouples from the radial component and describes a harmonic oscillation with the frequency ω_z in z-direction. Concerning the radial equations (see eq. (3.7) and eq. (3.8)) one can combine them with a new complex variable $u = x + iy$, to obtain

$$\ddot{u} + i\omega_c \dot{u} - \frac{1}{2}\omega_z^2 z = 0 \,. \tag{3.11}$$

The differential equation eq. (3.11) can be solved by the exponential ansatz $u = e^{-i\omega t}$, which results in a quadratic equation for ω

$$\omega^2 - \omega_c \omega + \frac{1}{2}\omega_z^2 = 0 \,. \tag{3.12}$$

Solving eq. (3.12) provides the two eigenfrequencies of the radial motion

$$\omega_\pm = \frac{1}{2}\left(\omega_c \pm \sqrt{\omega_c^2 - 2\omega_z^2}\right) , \tag{3.13}$$

where ω_+ is called the reduced cyclotron frequency and ω_- the magnetron frequency. A detailed discussion of the solutions of the radial components is presented in [Bro86]

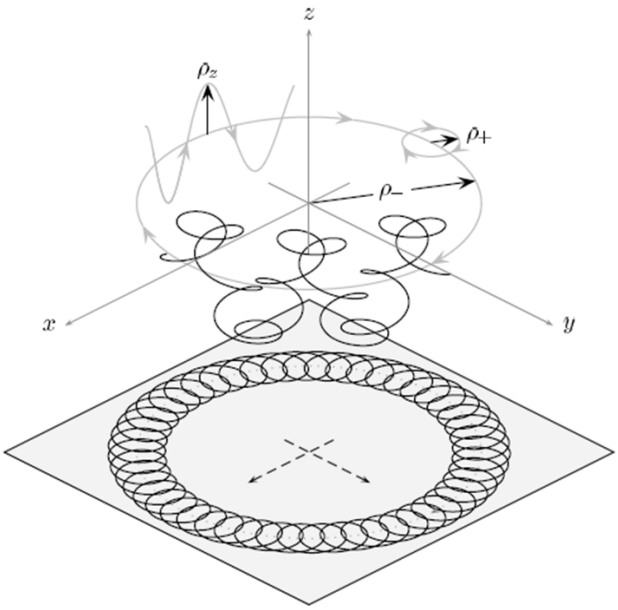

Figure 3.2: The superposition of the three different ion motions inside a Penning trap. The modified cyclotron motion with the high frequency ω_+ and the small radius ρ_+, the magnetron motion around the center of motion with ω_- and ρ_-, and the decoupled axial motion with frequency ω_z and amplitude ρ_z are visible.

and [Kre92]. The general solution to eq. (3.11) is given by

$$u(t) = A_+ e^{-i\omega_+ t} + A_- e^{-i\omega_- t}\,, \tag{3.14}$$

where the complex coefficients $A_\pm$ can be identified as the radii of the reduced cyclotron motion $\rho_+ = |A_+|$ and the magnetron motion $\rho_- = |A_-|$, respectively. Fig. 3.2 shows the superposition of all three motions.

Discussing the Solutions

In general, the frequencies differ by one or several orders of magnitude and are ordered by

$$\omega_c \approx \omega_+ > \omega_z > \omega_-\,. \tag{3.15}$$

Furthermore, a trapping condition can be derived from eq. (3.13):

$$\omega_c^2 - 2\omega_z^2 > 0\,, \tag{3.16}$$

which leads to

$$U_0 < \frac{qD^2}{2m} B^2\,. \tag{3.17}$$

A series expansion of eq. (3.13) leads to

$$\omega_+ \approx \omega_c - \frac{U_{dc}}{2D^2B} \quad \text{and} \tag{3.18}$$

$$\omega_- \approx \frac{U_{dc}}{2D^2B}\,. \tag{3.19}$$

It is worth noting that the magnetron frequency ω_- is in first order mass independent, whereas ω_+ and ω_z depend both on the mass and trap potentials. Furthermore, the frequencies obey the following relations:

$$\omega_z^2 = 2\omega_+\omega_-\,, \tag{3.20}$$

$$\omega_c = \omega_+ + \omega_-\,, \tag{3.21}$$

and

$$\omega_c^2 = \omega_+^2 + \omega_z^2 + \omega_-^2\,. \tag{3.22}$$

3.1.2 Real Penning Traps

Several imperfections have to be considered for real Penning traps, which influence the motion of the trapped ions and their eigenfrequencies. Both the electrostatic field and the magnetic field differ from the ideal case. However, for small imperfections one can still derive the correct ω_c, based on the frequencies $\overline{\omega}_z$, $\overline{\omega}_+$, and $\overline{\omega}_-$ of a real trap, as shown by the invariance theorem [Bro82]:

$$\omega_c^2 = \overline{\omega}_+^2 + \overline{\omega}_z^2 + \overline{\omega}_-^2\,. \tag{3.23}$$

Electric Field Imperfections

The solutions of the equations of motion of the ideal Penning trap were based on the assumption of infinite electrodes. This is not realizable for real Penning traps and hence, the electric field in a real Penning trap is not a perfect quadrupole field. Furthermore, bores in the endcaps, which allow the ions to enter and leave the trap, segmentations of the ring electrodes, and misalignments lead to field imperfections, which can be corrected partially by correction electrodes. Nevertheless, only an approximated quadrupole potential is present in the center of the trap and higher orders of the potential have to be taken into account.

Magnetic Field Imperfections

In real Penning traps, the eigenfrequencies can be shifted also due imperfections in the magnetic field. These can be caused by a misalignment of the magnetic field axis with respect to the symmetry axis of the trap and due to a magnetization by the strong magnetic field of the materials inside the trap.

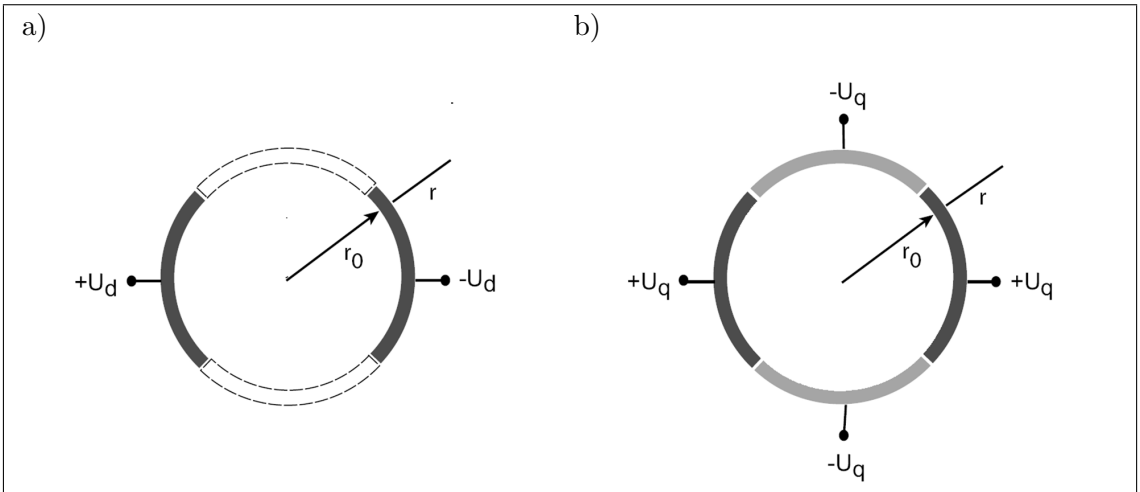

Figure 3.3: Cross section of a fourfold segmented ring electrode. a) For a dipole excitation, an rf-signal is applied to opposite segments with a voltage amplitude of $\pm U_d$. b) In a quadrupolar excitation, the phases are opposite on neighbouring segments.

3.1.3 Manipulation of the Ion Motion

Ion manipulation in a Penning trap is an essential part of all Penning trap experiments. From the quantum mechanics point of view ω_+, ω_-, and ω_z can be treated as single harmonic oscillators [Bro86]. All frequencies can be excited to higher states by irradiating a resonant frequency. Here, the magnetron motion has to be pointed out, since an excitation of ω_-, i.e. the increase of the magnetron radius ρ_-, leads to a lower level of potential energy. Several excitation modes are possible. At ISOLTRAP, the ion motion is manipulated by dipole and quadrupole excitation in the radial plane. For this purpose, the ring electrode is commonly segmented into equally size segments, as shown in fig. 3.3.

Dipole Excitation

The dipole excitation can address only one eigenmotion and is realized by applying an rf-signal with opposite phases to opposed ring segments as shown in fig. 3.3 a). An electric dipole field can be created by the following sinusoidal rf-potential:

$$\phi_d\left(x,t\right) = \frac{U_d}{a}\cos\left(\omega_d t + \theta_d\right)\cdot x\,, \tag{3.24}$$

where U_d is the amplitude of the applied voltage U_d, a the distance from a point in the trap to the trap center and ω_d the frequency of the rf-signal. The derived electric field has to be added to eq. (3.6). As a result, the solutions have the same form as eq. (3.14), but the magnetron radius ρ_- and the reduced cyclotron radius ρ_+ are time dependent now ($\rho_\pm \rightarrow \rho_\pm\left(t\right)$). One can show that when ω_d approaches ω_+ (ω_-), then the radius ρ_+

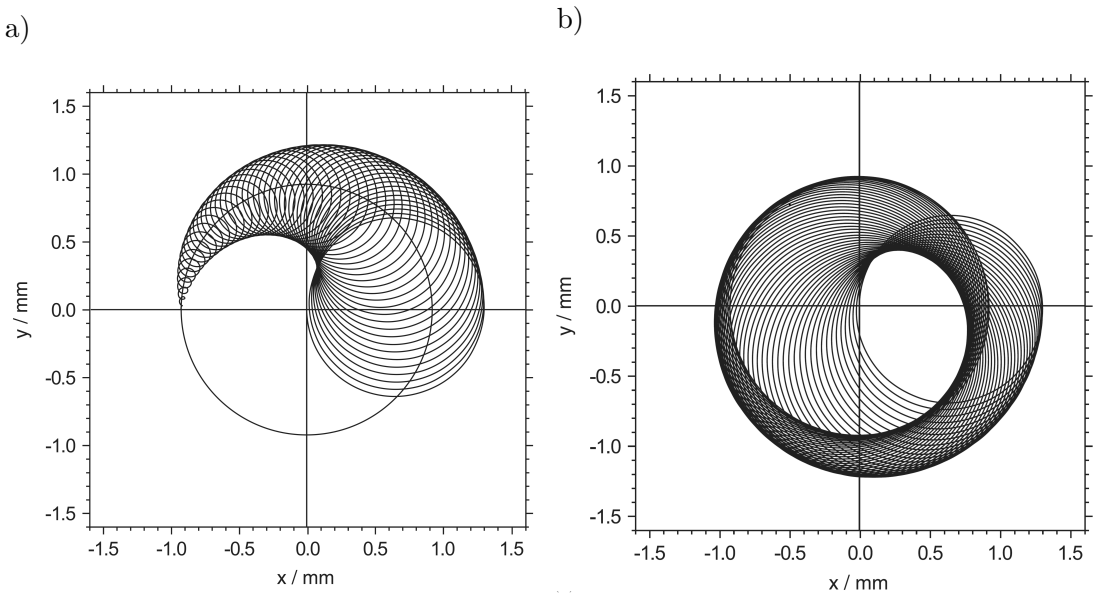

Figure 3.4: Trajectories of the ion motion in a Penning trap, in case a quadrupole excitation at ω_c is applied. The two pictures show a conversation of a pure magnetron motion into a cyclotron motion, where a) shows the first half of the conversion and b) the second half. [Bla06]

(ρ_-) resonantly increases. This allows resonant excitations of both radial eigenmotions. The procedure can be used to eject the ions radially from the trap.

Quadrupole Excitation

In the case of a quadrupole excitation, a sinusoidal rf-potential ϕ_q is applied to the segments as shown in fig. 3.3 b) and is given by

$$\phi_q(x,y,t) = \frac{U_q}{a}\cos(\omega_q t + \theta_q)\cdot\left(x^2 - y^2\right), \tag{3.25}$$

where U_q is the maximum potential of the quadrupole field measured on a circle with radius a. Similar to the dipole excitation, new trajectories are given with time dependent radii $\rho_\pm(t)$. The quadrupole excitation is used to couple two eigenfrequencies to each other. For instance, an excitation of $\omega_q = \omega_c = \omega_+ + \omega_-$ leads to a periodic conversion between the modified cyclotron motion and the magnetron motion (i.e. between ρ_- and ρ_+) and can be used for the determination of the cyclotron frequency ω_c. The period of such a conversion is given by [Kön95]

$$T_{conv} = \pi\frac{m}{q}\frac{2a^2}{U_q}(\omega_+ + \omega_-) \approx \pi\frac{2a^2}{2qU_q}B, \tag{3.26}$$

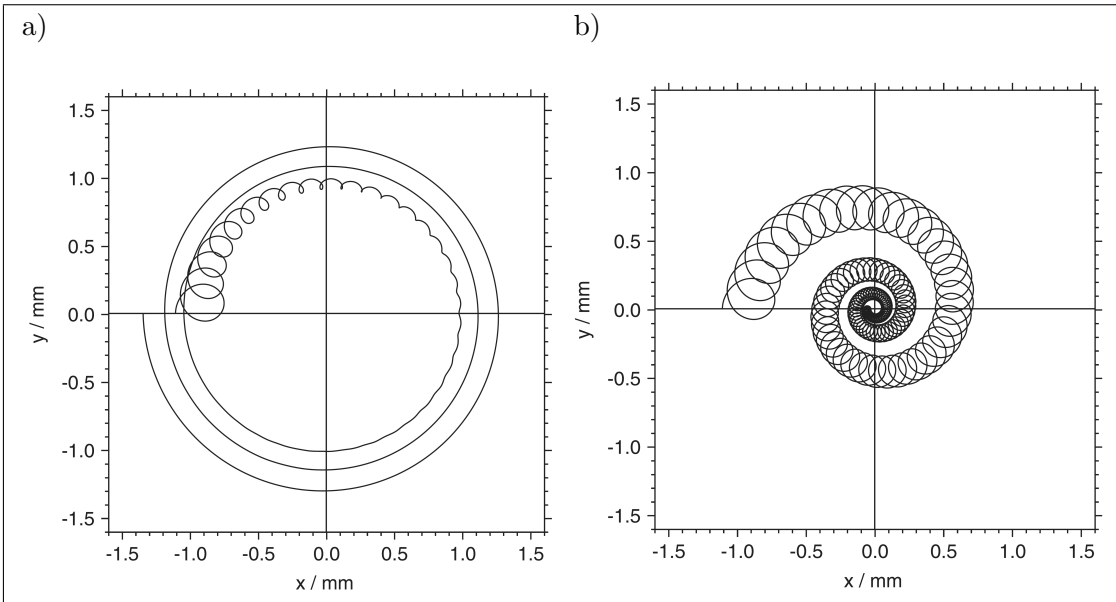

Figure 3.5: Simulations of an ion trajectory in a Penning trap filled with buffer gas [Sav91]. No excitation is applied in a). Here the decrease of the radius of the modified cyclotron frequency ρ_+ can be seen, while the magnetron radius ρ_- increases due the negative energy contribution. b) shows a combination of buffer-gas cooling and quadrupole excitation. Here, the ions are centered since the conversion of the two motions is faster than the increase of the magnetron radius. [Bla06]

which shows that the conversion depends in the first order only on the applied voltage U_q and the magnetic field B. Fig. 3.4 shows a simulation of a full conversion from a pure magnetron to a pure modified cyclotron motion.

Buffer-Gas Cooling and Purification

Buffer-gas cooling decreases the phase space distribution of a particle bunch [Sav91]. For this purpose light gas with a high ionization potential, usually helium is brought into the trap. It undergoes inelastic collisions with the ions and hence the particles loose kinetic energy. As a result, the emittance of the ion bunch is reduced. While ρ_+ and ρ_z decrease with every collision, ρ_- increases due to the negative energy contribution of the magnetron motion. The force can be described as friction via

$$\vec{F} = -\delta m \vec{v}\,, \tag{3.27}$$

where δ is the damping parameter. Fig. 3.5 a) shows a trajectory of a buffer-gas cooled ion. The purification from contaminants using buffer-gas cooling is performed in the following way: First, the ions are excited to a defined magnetron radius ρ_- by dipole

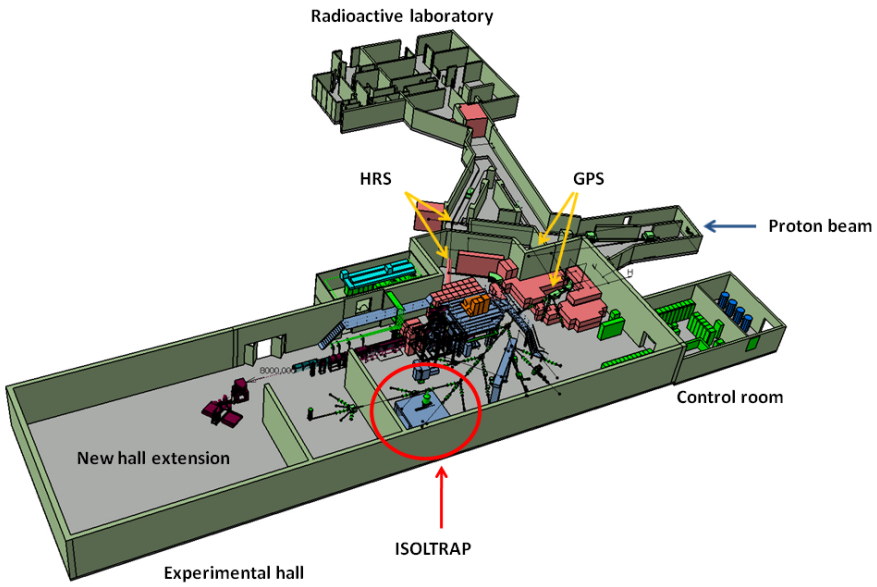

Figure 3.6: Overview over the ISOLDE experimental hall. The $1.0 - 1.4$ GeV proton beam coming from the PSB is shot on the targets. Afterwards, the produced atoms are ionized, accelerated to 60 keV, separated by the HRS or GPS magnets and guided to the experiments. ISOLTRAP is placed at the central beam line.

excitation at ω_-. Here, the whole ion cloud is excited, since the magnetron frequency is in first order mass independent, as described in chapter 3.1.1. Afterwards, the magnetron motion of the ions of interest is converted into cyclotron motion by the mass dependent quadrupole excitation at ω_c of the ions of interest. Due to the buffer-gas cooling, the radius of the cyclotron motion is damped quickly and only these ions are brought towards the trap center with a small radius. Fig. 3.5 b) illustrates this process. When the ions are ejected, only the centered ions with small radii are able to pass a small diaphragm at the top of the trap, while the non-excited ions remain at a larger radius and hit the diaphragm.

3.2 The ISOLTRAP Experiment

3.2.1 The ISOLDE Facility

The ISOLDE facility [Kug00] at CERN in Geneva, Switzerland is devoted to the production and on-line separation of exotic, short-lived radionuclei. Many experiments in atomic and nuclear physics, solid-state physics, life-science, and material science located at ISOLDE benefit from its beams. Fig. 3.6 gives an overview over the ISOLDE experimental hall and its main parts. The radioactive nuclei are produced by fission, spallation or fragmentation in a thick high-temperature target. Therefore, a very short, $1-1.4$ GeV proton bunch, delivered by the PSB (Proton Synchrotron Booster) is impinged on the

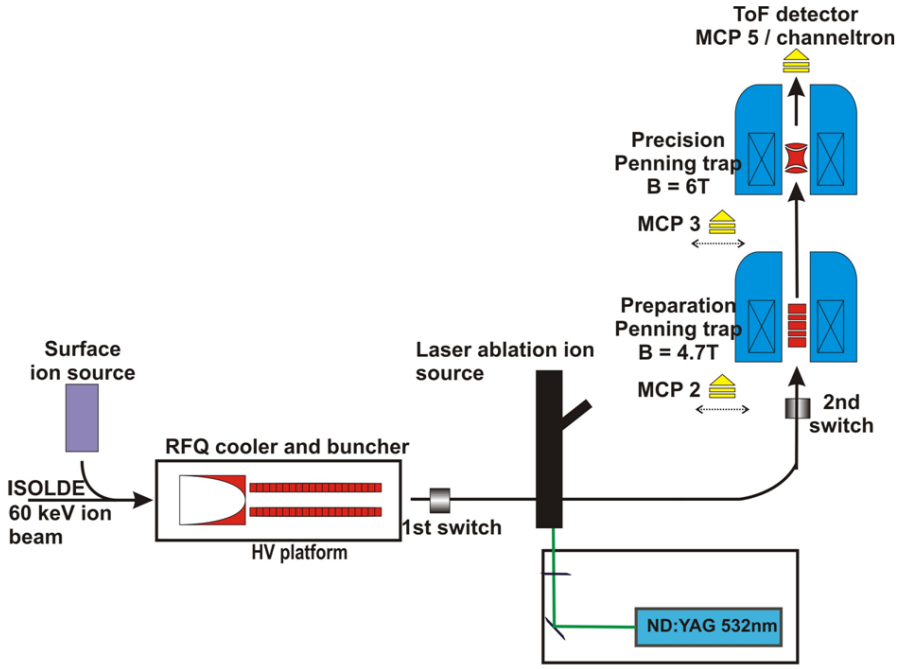

Figure 3.7: Sketch of the ISOLTRAP setup. The three traps are shown, as well as the two off-line ion sources and the most important ion detectors.

target every 1.2 s or its multiples. Afterwards, the isotopes diffuse from the hot target into an ion source. Here, the isotopes are ionized by surface, plasma, or resonant laser ionization (RILIS), depending on the chemical or physical properties and possible isobaric contaminations [Kös03]. Presently, more than 70 elements and around 1100 isotopes are accessible at ISOLDE. Next, the ions are accelerated to $30 - 60$ keV and mass separated by one of two magnetic mass separators. The general purpose separator (GPS) works with a 90° magnet with $B = 0.45$ T and a resolution of $R \approx 2400$, while the high resolution separator (HRS) can reach a resolution of $R \approx 7000$ by two magnets with 60° and 90°, and a magnetic field of $B = 0.7$ T. Last but not least, the ions are guided to the different experiments by ion optics, based on electrostatic lenses and deflectors.

3.2.2 The ISOLTRAP Setup

The ISOLTRAP setup is located at the central beamline of ISOLDE [Muk08]. Spread over two floors, the experiment consists of three main traps, namely the radiofrequency quadrupole (RFQ) cooler and buncher, the preparation Penning trap and the precision Penning trap. Fig. 3.7 shows an overview of the setup. The investigated ions are delivered either by one of the two off-line ion sources (surface-ionization or laser-ablation source) or by ISOLDE. First, the ions of the surface ion source or ISOLDE reach the RFQ, which decelerates, cools and accumulates the ion beam. The ions of the laser ablation

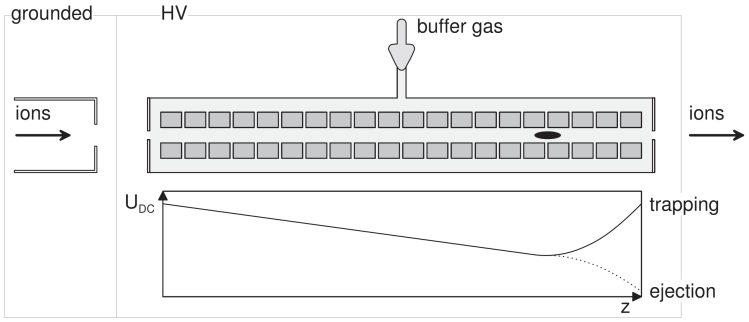

Figure 3.8: Sketch of the ISOLTRAP ion cooler and buncher. The ion beam is decelerated by an injection electrode, radially confined by an rf-potential and accumulated at the end of the buncher in an axial dc-trapping potential. The scheme below shows the axial potential, which can lowered at the end for the ejection of the ion bunch. [Her01]

source are injected into ISOLTRAP behind the buncher. Afterwards, the ion bunch is injected into the preparation trap, where the beam is purified from possible isobaric contaminations. At last, the cyclotron-frequency measurement and hence, the mass determination is performed in the precision trap by the TOF-ICR method (see section 3.2.3). Several micro-channel plate detectors (MCP) can be moved at various places into the beamline to optimize the ion beam transfer, whereas the final measurement is performed either by an MCP or by an electron multiplier [Yaz06], which has a higher detection efficiency than an MCP. The laser-ablation ion source was modified within this thesis and used for the ionization of ^{110}Cd and ^{110}Pd for the measurements of their masses and of their Q-value.
Chapter 4 describes the modifications in detail, whereas the present chapter presents the parts of the experimental setup.

Radiofrequency Ion Beam Cooler and Buncher

The radiofrequency ion beam cooler and buncher (RFQ) is the first trap of ISOLTRAP, which cools, accumulates and bunches the semi-continuous ion beam from ISOLDE in order to prepare the ions for the further traps [Her01]. The buncher is based on the Paul trap technique combined with buffer-gas cooling. Fig. 3.8 shows a scheme of the ISOLTRAP ion cooler and buncher. An injection electrode decelerates the $30 - 60$ keV ion beam down to 100 eV and injects it into the RFQ. The trap consists of four segmented rods to which one applies an rf-potential, which confines the ions in radial direction and a dc-field for confinement in axial direction. The helium buffer gas with a pressure of about 10^{-6} mbar dissipates the kinetic energy of the ions and cools them. Finally, the ions accumulate in a potential minimum at the end of the trap. After a cooling time of several milliseconds, the dc-potential at the end of the trap is lowered and the ions are ejected with an energy of about 2.8 keV towards the ISOLTRAP beam line. In total, the

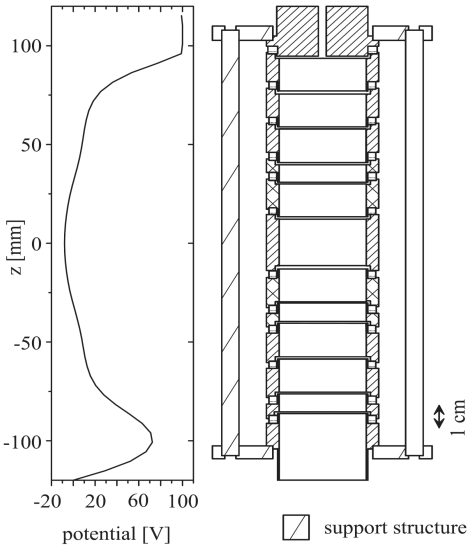

Figure 3.9: The ISOLTRAP preparation Penning trap and the resulting axial trapping potential. The diaphragm used for blocking the isobaric contaminants is shown to the right. [Muk08]

ion emittance can be reduced from around $\epsilon \approx 35\pi$ mm mrad to $\epsilon \approx 2\pi$ mm mrad, which allows an efficient transport of the ions and a good capture in the preparation trap.

Preparation Trap

After the ejection from the RFQ, the ions are focused and deflected towards the preparation Penning trap [Bec93], whose task is to clean the ion beam from isobaric contaminations and to prepare the ions for a further transport to the precision Penning trap. This cylindrical Penning trap is placed in a superconducting magnet of about $B = 4.7$ T. To store the ions in the axial direction, the ring segments generate a potential as shown in fig. 3.9. Additionally, helium at a pressure of 10^{-4} mbar is let in for buffer-gas cooling and damping. The isobaric cleaning is performed as described in chapter 3.1.3. Typical excitation times in this trap are around 30 ms for the dipolar excitation and 50-150 ms for the quadrupolar excitation. Fig. 3.10 shows a simulation of cleaning away $^{106}Cd^+$ from the $^{106}Pd^+$ beam. The C++ program solves the equations of motion of the ions in the preparation trap and visualizes the behavior of the ion parameter such as the particle position and the cyclotron and magnetron radius. In this example, the cyclotron frequency of $^{106}Pd^+$ is applied to the preparation Penning trap and only the $^{106}Pd^+$ ions are brought to the trap center with a radius lower than the diaphragm radius. Fig. 3.11 shows a scan of the quadrupole frequency around the cyclotron frequency of the two isobars $^{108}Pd^+$ and carbon cluster $^{12}C_9^+$. Only if the quadrupole frequency matches one of the cyclotron frequency, ions are detected behind the preparation trap. The overall obtained resolving power is 56000.

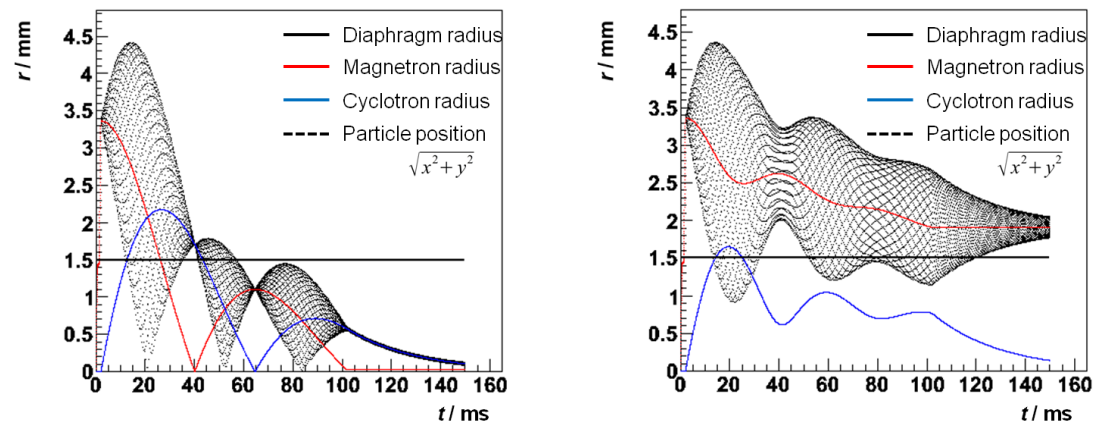

Figure 3.10: An example of the purification process in the preparation Penning trap with $^{106}Pd^{+}$ and $^{106}Cd^{+}$. Both ion species are rapidly excited to a magnetron radius of about 3.4 mm by a mass independent dipole excitation at ω_{-}. Afterwards, a quadrupole excitation at ω_c of $^{106}Pd^{+}$ is applied. As a result, only the magnetron motion of $^{106}Pd^{+}$ is converted fully into a cyclotron motion and the radius of $^{106}Pd^{+}$ is quickly damped below the radius of the diaphragm. The conversion for $^{106}Cd^{+}$ is only partial and thus this ion remains at a larger radius and hits the diaphragm when ejected.

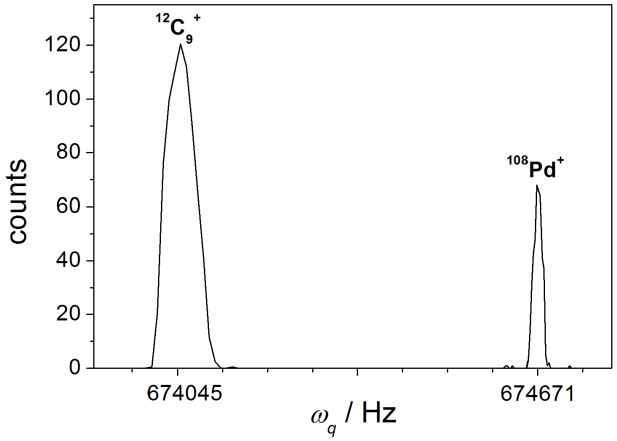

Figure 3.11: This picture shows the ion number as a function of the quadrupole frequency ω_q around the cyclotron frequencies ω_c of the two isobars $^{108}Pd^{+}$ and carbon cluster $^{12}C_9^{+}$. Resonances are obtained, if the quadrupole frequency matches the cyclotron frequency of one of the isobars, while no ions are able to pass the preparation trap, if the quadrupole frequency is out of resonance.

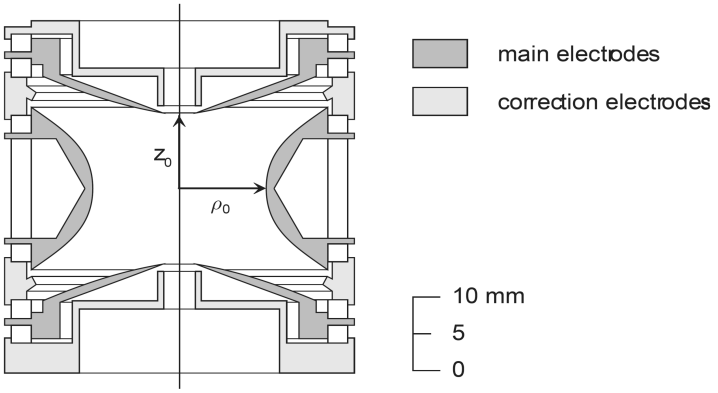

Figure 3.12: Sketch of the hyperbolic Penning precision trap. The main elements are the ring electrodes and the end caps. [Muk08]

Precision Trap

After isobaric cleaning, the ions are transferred to the hyperbolic Penning trap, namely the precision trap, where the cyclotron frequency is determined. A schematic drawing is shown in fig. 3.12. The trap is placed in a magnetic field of $B = 5.9\,\mathrm{T}$, provided by a superconducting magnet. After a good preparation of the ions in the preparation trap, the ions have a very low energy spread and are close to the magnetic field axis. Thus, when trapped in the precision trap, the ions have almost no reduced cyclotron radius ($\rho_+ \approx 0$) and a very small magnetron radius ($\rho_- \approx 0.2\,\mathrm{mm}$). No buffer gas is present in the precision trap and the vacuum is of the order of $10^{-9}\,\mathrm{mbar}$. The cyclotron frequency is determined using the ToF-ICR method, described in section 3.2.3. Typical excitation times are around 10 ms for the dipole excitation and 100 ms up to several seconds for the quadrupole excitation depending on the required resolution and precision aimed for.

3.2.3 Ion Detection and Determination of ω_c by the Destructive TOF-ICR Detection

The cyclotron frequency ω_c is the parameter of interest in Penning trap mass spectrometers and several methods depending on the requirements of the experiment were developed to measure this quantity. At ISOLTRAP, the measurement of ω_c is based on the destructive time-of-flight ion cyclotron resonance (TOF-ICR) detection technique [Grä80]. For this purpose an ion detector is placed after the Penning trap for the time-of-flight (ToF) measurement. At ISOLTRAP, either a micro-channel plate or an electron multiplier detector is in use. First of all, the ions are excited to a defined magnetron radius, using a phase-locked dipole excitation at ω_- [Bla03]. This leads to a magnetron radius of around $\rho_- = 0.7\,\mathrm{mm}$. At this stage, the ions have a relatively low orbital magnetic moment μ due to their low frequency. Next, a quadrupolar excitation around ω_c is performed. In case of resonance ($\omega_q = \omega_c$), the magnetron motion is fully

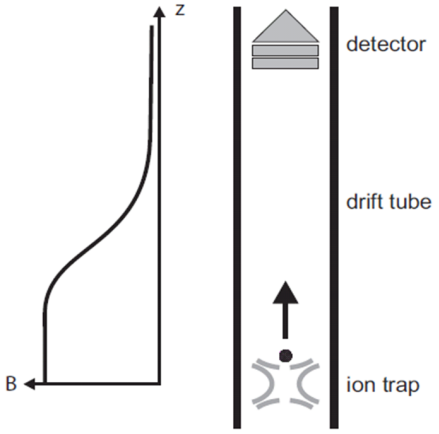

Figure 3.13: The main elements of the TOF-ICR detection are shown. In the left picture, the field profile of the magnetic field is shown qualitatively. The ions are ejected from the Penning trap into the drift tube towards the ion detector (MCP or electron multiplier) as shown in the right picture [Grä80].

converted into a modified cyclotron motion (if the excitation time T_q and the amplitude U_q are choosen accordingly), otherwise, if $\omega_q \neq \omega_c$ the conversion is only partial. In the experimental procedure, several frequencies in a range around the expected cyclotron frequencies are applied. During the conversion, the radial energy increases by several orders of magnitudes and so does the magnetic moment μ of the trapped ion. This increase is probed in the following way: The trap potential is lowered and the ions drift out of the trap towards the ion detector. Outside the trap, the ions interact with a strong magnetic field gradient and thus, are accelerated by the gradient force, which is proportional to the magnetic moment and given by

$$\vec{F} = -\vec{\mu}\left(\vec{\nabla}\vec{B}\right) = -\frac{E_r}{B}\frac{\partial B}{\partial z}\hat{e}_z\,, \tag{3.28}$$

whereas $E_r = |\mu|\,|B|$ is the radial energy of the particle. Fig. 3.13 illustrates the principle. Since the magnetic moment and the radial energy are maximal in case of a full conversion from ω_- to ω_+, the force is the strongest in resonance, i.e. if $\omega_q = \omega_c$. Hence, the time of flight from the trap to the detector, which is the measured quantity in TOF-ICR, is shortest. The ToF spectrum can be described theoretically by [Grä80]

$$T_{tot}\left(\omega_q\right) = \int_0^{z_1} \sqrt{\frac{m}{2\left(E_{z0} - q\cdot U\left(z\right) - \mu\left(\omega_q\right)\cdot B\left(z\right)\right)}}\,dz\,, \tag{3.29}$$

where z_1 is the distance from the trap center to the detector, E_{z0} the initial axial energy, $U\left(z\right)$ is the electric potential created by the electrodes along the z-axis, and $B\left(z\right)$ is the magnetic field along the z-axis. A resulting ToF resonance of $^{87}Rb^+$ and the

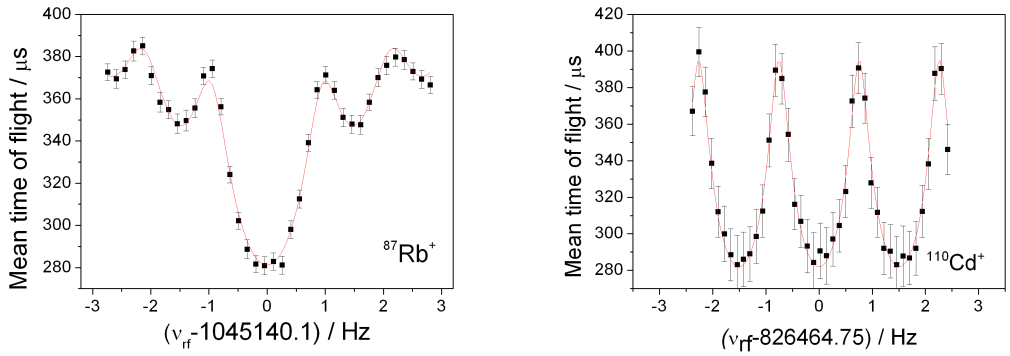

Figure 3.14: a): A ToF-ICR spectrum of $^{87}Rb^+$ with the quadrupole excitation time of $T_q = 900\,\text{ms}$. The theoretically expected line-shape is fitted to the data [Grä80]. b): A Ramsey ToF-ICR spectrum of $^{110}Cd^+$ with an excitation sequence of $((50 - 600 - 50)\,\text{ms}$. The sidebands are much more pronounced than with the conventional excitation. The solid line is a fit to the data [Kre07]. For more details see text.

corresponding fit of eq.(3.29) is shown in fig. 3.14 a). The resolving power R is determined by the quadrupole excitation time T_q and given by [Bol96]

$$R = \frac{m}{\Delta m} = \frac{\omega_c}{\Delta\omega_c} \approx \frac{\omega_c}{2\pi} T_q\,, \tag{3.30}$$

where $\Delta m = |m_1 - m_2|$ is the minimum mass difference which can be distinguished and $\Delta\omega = |\omega_1 - \omega_2|$ is the corresponding frequency different of the two masses. An alternative variation of the TOF-ICR method is the Ramsey excitation. Here, two pulses of quadrupole radiation (which have in the present studies the same duration τ_1) around ω_c, separated by a waiting time τ_0 are used. As a result, the sidebands of the ToF resonance become more pronounced and hence, the resolving power increases with a factor of about two comparing to a single excitation with the same excitation time $T_q = 2 \cdot \tau_1 + \tau_0$. Fig. 3.14 b) shows a Ramsey spectrum of $^{110}Cd^+$, measured with $\tau_1 = 50\,\text{ms}$ and $\tau_0 = 600\,\text{ms}$ in the following referred as a $(50 - 600 - 50)\,\text{ms}$ sequence. A detailed description of this approach is given in [Kre07, Geo07].

4 Modification and Characterization of the ISOLTRAP Laser Ion Source

Presently, two off-line ion sources are installed at ISOLTRAP to provide ions as references for mass measurements, to optimise the setup, and for off-line experiments. As shown in fig. 3.7, the surface ion source is mounted next to the beamline of ISOLDE in front of the radiofrequency buncher. The laser ablation ion source is the second off-line source and is built in between the buncher and the preparation trap. The ISOLTRAP surface ion source is able to produce continuous stable ion beams of alkali elements, such as ^{39,41}K, ^{85,87}Rb and ^{133}Cs. The laser ion source was recently installed and was mostly used to study the accuracy of ISOLTRAP with carbon clusters [Kel03]. In 2008, it was modified to provide carbon clusters as reference masses [Böh09]. Within this thesis, several more modifications were performed to stabilize the ion production, to optimize the handling of the source, and to improve the starting conditions of the ions. With the new setup, cadmium, palladium, and carbon clusters could be produced successfully. The present chapter regards the laser ablation principle, the ion source modifications, and the resulting ion spectra.

4.1 Brief Introduction to Laser Ablation

Laser ionization at ISOLTRAP is performed by laser ablation, where a high-energy laser pulse is focused on a solid target, vaporizes some material, and creates a plasma plume. This process is highly non-element specific in contrast to the resonant ionization laser ion sources (RILIS). The physics of laser ablation is still not fully understood and no final explanation of the expansion and the energy distribution of the ablated particles is given [Mau04]. In general, the most important parameters in that process are the pulse duration, the energy, the wavelength, and the spatial energy profile of the laser beam [Rus04]. Short wavelengths give higher ablation efficiency, while longer wavelengths lead to higher kinetic energies in the plume [Tor03]. Laser ablation exhibits non-linear behavior as a function of the laser power density and several effects dominate for different ranges of the laser power density (see fig. 4.1 a). Low energy effects may be dominated by thermal effects (1), followed by plasma absorption at an higher energy (2), up to phase explosion (3), and an high energy plasma (4) [Rus04]. As a result, the laser ablation properties such as the mass ablation rate, plasma temperature, particle size distribution, and particle chemistry will be different in each of these regions. At low energies, only neutral atoms are produced, until at a certain threshold energy, the ions start to appear. Here, the threshold depends on the material. Gadolinium, for instance, has an ablation threshold of about 0.15 J/cm^2 and an ionization threshold of

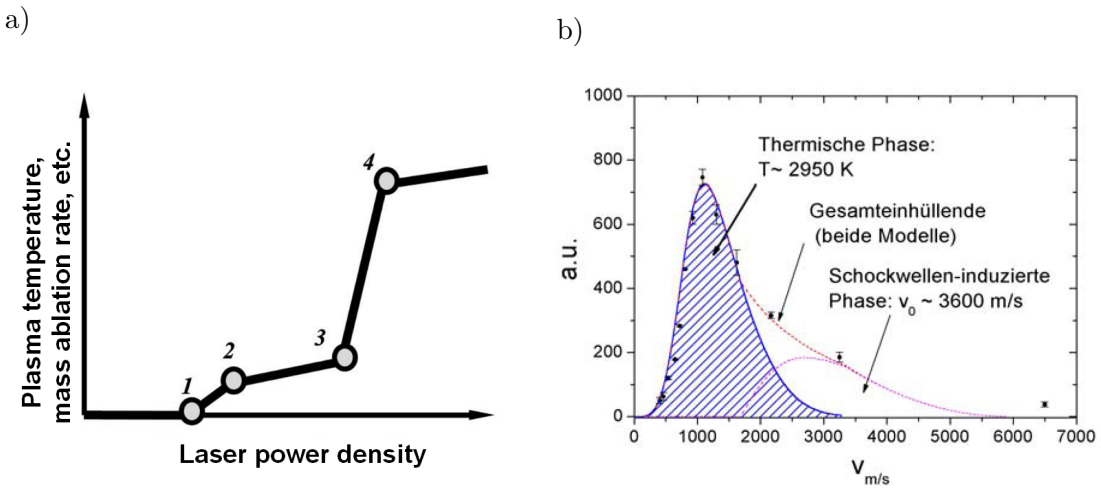

Figure 4.1: a) Laser ablation properties (e.g. plasma temperature, mass ablation rate, plasma temperature or particle size distribution) as a function of the laser power density. Four laser power density intervals are dominated by 1) thermal effects, 2) plasma absorption 3) phase explosion and 4) high energy plasma [Rus04]. b) Velocity distribution measured for laser ablated gadolinium. The resulting energy distribution is the envelope of a Maxwell velocity distribution and the phase explosion phase [Mau04].

about 0.2 J/cm^2 [Mau04]. In general, single and higher charged ions can be produced as well as charged clusters. The velocity distribution is of special interest for ion transport and its simulation since it defines the starting conditions of the ions. Fig. 4.1 b) shows the velocity distribution in the neutral ablation phase of gadolinium. Here, a simple Maxwell distribution is not sufficient, since the faster ions are dominated by the phase explosion [Mau04, Rus04]. As a result, the energy distribution can be described by an envelope of a Maxwell velocity distribution and the phase explosion phase.

4.2 Current Setup of the ISOLTRAP Laser Ablation Source and its Recent Modifications

The laser ablation ion source at ISOLTRAP consists of three main parts: The laser system, the sample holder, and the ion optics. Fig. 4.2 shows a sketch of the main elements. The laser system consists of a nanosecond-pulse, frequency-doubled 532 nm Nd:YAG laser, which can provide laser light pulses of ns width, two beamsplitters, three mirrors and a lens with a focus length of 700 mm. The first beam splitter is used to attenuate the laser power additionally to the laser control. The second one is used to reflect a small fraction of $E = 3.35\,\%$ of the total energy to an energy meter to monitor the irradiated laser energy. After passing the lens, the laser beam goes through an entrance window into the vacuum chamber of ISOLTRAP where it hits the pellet at

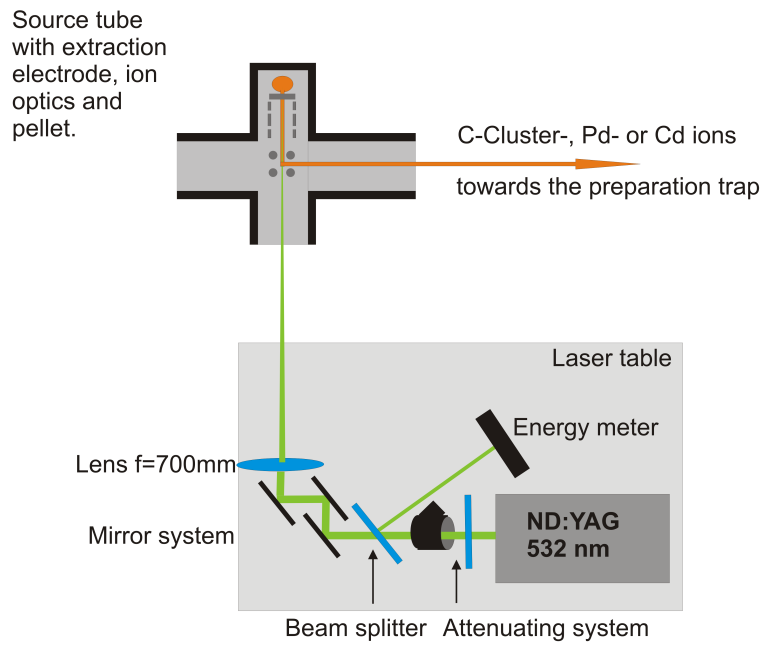

Figure 4.2: The main parts of the laser ion source at ISOLTRAP. The light from a pulsed, frequency-doubled 532 nm Nd:YAG laser goes through a beam attenuator, beam splitter, several mirrors, and through a 700 mm lens before reaching the sample holder with SIGRADUR©, palladium and cadmium segments, respectively. The ions are guided towards the preparation trap. The dimensions are not to scale.

the end of the source tube. Here, a glassy carbon pellet (SIGRADUR©), a palladium foil and a cadmium foil are put on a rotatable sample holder, which allows to choose position selective between the different elements. Afterwards, the ions are extracted into the source tube, focussed and guided into the ISOLTRAP beam line towards the preparation trap by the ion optics.

4.2.1 Laser System

The Laser

Presently, a Polaris II© frequency-doubled 532 nm Nd:YAG laser from New Wave Research is in use. The laser is able to provide repetition rates from $1 - 10$ Hz with a pulse length of $3 - 4$ ns. The maximum pulse energy at the laser output was about 26 mJ/pulse and at the probe position in the vacuum chamber about 20.3 mJ/pulse. In the following, the laser energy means always the energy at the probe position. The beam diameter at the output is $d = 2.75$ mm with a divergence below 3.5 mrad. To attenuate the laser energy, the laser has an internal optical attenuator, which consists of a half-wave plate and a polarizer. Within this thesis, this laser was installed to replace the previous frequency-doubled 532 nm Nd:YAG laser (Quantum Brilliant B©). The laser

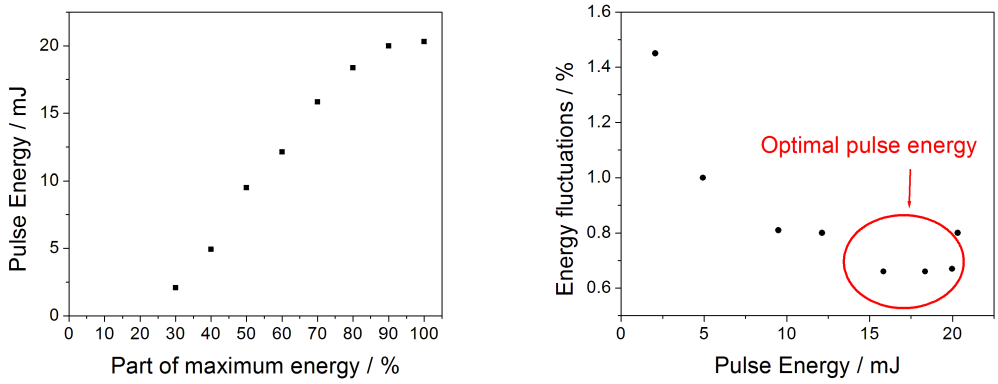

Figure 4.3: a) Polaris II© pulse energy as a function of the internal optical attenuator. The maximum energy at the position of the probe was 20.3 mJ/pulse. b) The relation between the pulse energy and the pulse-to-pulse energy fluctuation. The lowest fluctuations were measured in the region between 13 mJ/pulse and 19 mJ/pulse.

stabilities of both lasers were compared (using OPHIR PE25© energy meter), since the energy per laser pulse is a crucial parameter in the ion production. The former laser in use, the Quantum Brilliant B© laser showed pulse-to-pulse energy fluctuations of 5 % at a pulse energy of $E = 72$ mJ. The fluctuations increase to 8 %, if the pulse energy is attenuated down to normal operating energies at ISOLTRAP of $3 - 20$ mJ. The same measurement with the Polaris II© laser led to a fluctuation of only 0.7 % at a typical energy around 18 mJ/pulse, as shown in fig. 4.3 b). Furthermore, the old laser showed a slightly defective beam profile. At present, the Polaris II© laser runs at an energy around 18 mJ/pulse in order to provide the best pulse-to-pulse stability. If attenuation is needed, a second optical attenuator consisting of a half-wave plate and a polarizer is placed in front of the laser, as described in the next chapter. Furthermore, the laser is connected to a frequency generator, in order to control the repetition rate externally. This allows to decrease the repetition rates for longer measurement cycles. Typically, repetition rates of 0.5 Hz were used.

Laser Optics

The ion source laser optic consists of an attenuating system, a beam splitter, an energy meter, three mirrors, and a lens with a focus length of $f = 700$ mm. The attenuator lowers the pulse energy additionally to the internal optical attenuator of the laser. It consists of a half-wave plate and a polarizing beam splitter. The first changes the polarization direction of the linearly polarized laser light by a certain angle. The latter is sensitive to the polarization direction and splits the linearly polarized beam into its

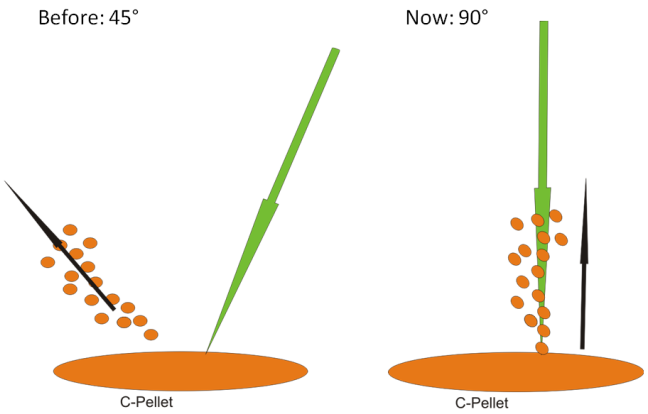

Figure 4.4: Previously, the laser was shot on the sample holder at an angle of 45°, whereas now the laser is shot perpendicular on the pellet. As a result, the ions are injected into the ion beam line with better starting conditions and the handling of the laser spot position is improved. This conclusion was obtained by simulations with SIMION^{copyright} as discussed in section 4.2.3.

vector components. By changing the polarization angle, the laser transmission can be controlled. In order to monitor the laser energy continuously, a glass beam splitter was added to the laser beam line, which reflects a small fraction of the laser energy (3.35 %) towards an OPHIR PE25© energy meter. In addition, a three-mirror system was placed into the laser beam, which allows to align the laser beam precisely. One of the main modifications during this thesis, was the change of the entrance angle of the laser beam from 45° degrees to the pellet surface to now, perpendicular on the sample holder. Therefore, the whole laser beam line as well as the ion source tube had to be modified. As a result, the ions are ejected along the ion optics axis, now and hence, have better starting conditions. Furthermore, the position of the laser spot is much easier to control now. The modification is illustrated in fig. 4.4.

Laser Focus

The determining parameter in the laser ablation process is the laser power density since the ion production responds sensitively to the laser energy deposited in the target. No ions are obtained under a certain laser power density threshold, whereas the ion production decreases rapidly, if the laser power density is too high. Furthermore, in case of carbon cluster production, the relative production of different cluster sizes depends also on the laser power density. In order to determine the irradiated laser power density, the radius of the laser focus was determined by the knife-edge method for several laser energies [Wri92]. Here, a sharp-edged object, in this case a razor blade, is moved

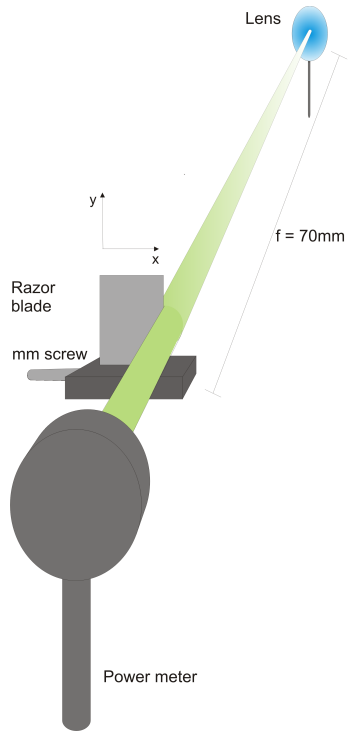

Figure 4.5: An illustration of the knife-edge method for laser radius determination. A razor blade is fixed on a small micrometer table and is moved through the laser beam, while the transmitted laser power is measured by a power meter. The same procedure was repeated in the vertical direction.

through the laser beam and blocks partly the beam. The beam radius is determined by measuring the transmitted laser power at several positions of the razor blade. Fig. 4.5 illustrates the experimental setup and the method. Several knife positions in horizontal and vertical direction were chosen for four laser energies. Afterwards, the data was fitted as discussed below: The radius of a Gaussian beam can be defined as the distance from the center of the beam with the maximum intensity I_0 to the position where the intensity drops to I_0/e^2. In the following discussion, a Gaussian beam with a propagation in z-direction is assumed. Then, the intensity profile in horizontal and vertical direction is given by [Cha93]

$$I(x,y) = I_0\, e^{\left(-\frac{2(x-x_0)^2}{w_x^2} - \frac{2(y-y_0)^2}{w_y^2}\right)}, \tag{4.1}$$

where I_0 is the maximum intensity of the beam in the beam center, w_x and w_y the $1/e^2$ beam radius in x- and y-direction and x_0 and y_0 the initial positions of the razor blade in the x- (horizontal) and y- (vertical) direction. Then, the total power of a laser beam

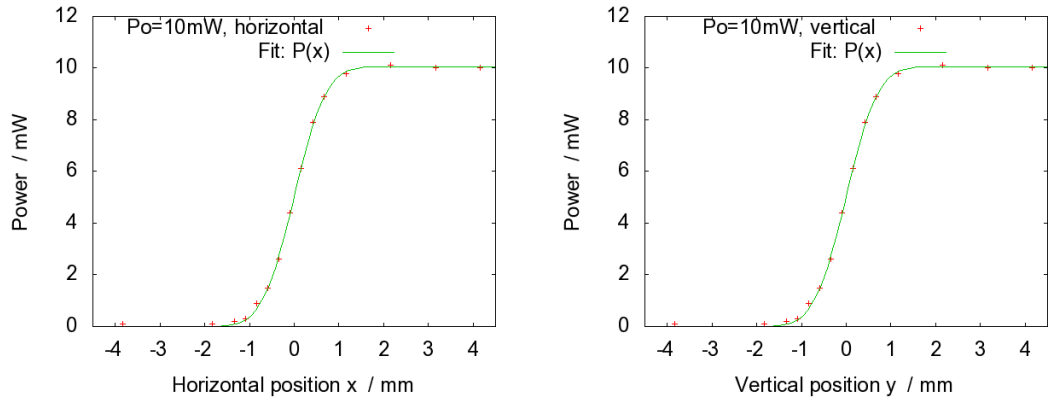

Figure 4.6: a) Results of the horizontal measurement at a laser energy of 10 mJ. The dashed line is a fit of eq. (4.4) to the data. b) The same in vertical direction.

can be calculated by

$$P_{tot} = I_0 \int_{-\infty}^{\infty} dx\, e^{-\frac{2(x-x_0)^2}{w_x^2}} \int_{-\infty}^{\infty} dy\, e^{-\frac{2(y-y_0)^2}{w_y^2}} \,. \tag{4.2}$$

Considering the knife edge being moved through the beam in x-direction as shown in fig. 4.5, the transmitted power is given by

$$P\,(x) = P_{tot} - I_0 \int_{-\infty}^{x} dx\, e^{-\frac{2(x-x_0)^2}{w_x^2}} \int_{-\infty}^{\infty} dy\, e^{-\frac{2(y-y_0)^2}{w_y^2}} \,, \tag{4.3}$$

which leads to

$$P_{tot}\,(x) = \frac{P_{tot}}{2}\left[1 + \mathrm{erf}\left(\frac{\sqrt{2}\,(x-x_0)}{w_x}\right)\right] , \tag{4.4}$$

where erf (...) is the Gaussian error function. The same formula is obtained in the vertical direction. Since the measurements were performed at a pulse repetition rate of 1 Hz, the total power P_{tot} is equivalent to the laser pulse energy E_{pulse}. Fig. 4.6 shows the measurements in horizontal and vertical direction with a laser pulse energy of about 10 mJ. The same procedure was repeated with laser pulse energies of about 5 mJ, 15 mJ, and 20 mJ. After fitting the data, the total laser pulse energy E_{pulse}, the radius in horizontal w_{hor}, and the radius in vertical direction w_{ver} could be obtained and finally used to calculate the laser power density ρ in the focus at the sample by

$$\rho = \frac{E_{pulse}}{T_{pulse} \cdot A_{focus}} = \frac{E_{pulse}}{T_{pulse} \cdot \pi \cdot w_{hor} \cdot w_{ver}} \,, \tag{4.5}$$

where T_{pulse} is the laser pulse duration time and A_{focus} is the area of the laser beam in the focus. Approximating the laser focus shape by an ellipse with $A_{ellipse} = \pi \cdot w_{hor} \cdot w_{ver}$ leads to

$$\rho = \frac{E_{pulse}}{T_{pulse} \cdot \pi \cdot w_{hor} \cdot w_{ver}} \,. \tag{4.6}$$

Tab. 4.1 shows the results. The laser beam has a slightly elliptic beam profile with a ratio of $w_{ver}/w_{hor} = 1/1.18$ between the vertical and horizontal direction. Furthermore, the obtained radii of the different measurements agree within the errors and no change of the radius could be determined for different laser pulse energies. Using the results

Table 4.1: The results of the beam radius measurements obtained by the knife edge method. The evaluated maximum energy per pulse E_{pulse} and the radii in horizontal w_{hor} and vertical direction w_{ver} were obtained by fits of eq. (4.4) to the experimental data. Using these parameters, the laser power densities ρ were calculated.

E_{pulse} / mJ	w_{hor} / mm	w_{ver} / mm	ρ / W/cm^2
4.8	1.44 ± 0.10	1.21 ± 0.09	$2.50 \cdot 10^7$
10.1	1.33 ± 0.07	1.12 ± 0.07	$6.17 \cdot 10^7$
14.6	1.37 ± 0.08	1.17 ± 0.08	$8.28 \cdot 10^7$
19.6	1.45 ± 0.07	1.23 ± 0.09	$1.00 \cdot 10^8$

shown in tab. 4.1, the irradiated laser power density ρ can be extrapolated to other laser pulse energies E_{pulse} given in J by

$$\rho\,(E_{pulse}) = 5.52 \cdot 10^9 \cdot E_{pulse} \,\left(1/\mathrm{s} \cdot \mathrm{cm}^2\right) \,. \tag{4.7}$$

In the following, an error of the irradiated laser power density of 5 % is assumed.

4.2.2 Sample Holder

The sample holder consists of an aluminum disc, which is connected to a rotatable feed through by an insulator. A circular recess with a diameter of 15 mm and a depth of 1 mm is countersinked into the aluminum disc, where the carbon pellet can be inserted. In this way the surface of the probe pellet is at the same height as the disc, which reduces the disturbances of the electrostatic field. Here, the carbon pellet is glued into the dent by a conducting silver-doped two component epoxy clue. The palladium and cadmium pieces are glued on the carbon pellet as shown in fig. 4.7, so that all three elements are arranged in three 120° segments. The aluminum disc is rotated manually or by a motor in order to change the position of the laser spot on the target or to change the target material. The electric potential of the aluminum disk defines the starting energy of the ablated ions. For this reason, the sample holder disc is in contact with the ball-bearing, connected to the formation chamber. The ball-bearing allows the pellet to be turned and to be conductively connected to the formation chamber at the same

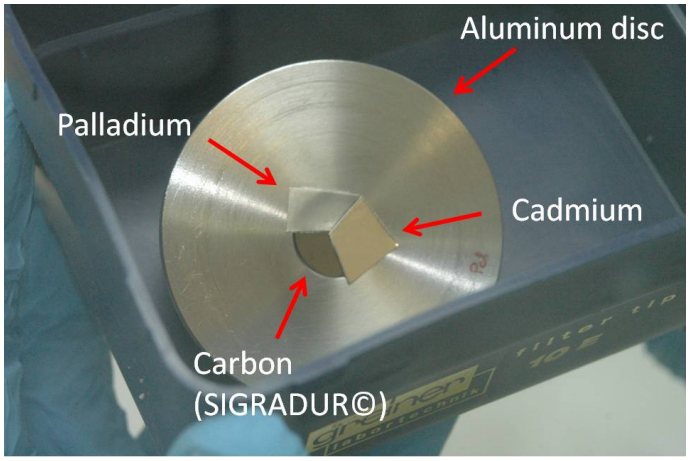

Figure 4.7: A photograph of the aluminum disc and pellet. The carbon pellet is glued into the dent with a conducting silver doped two component epoxy clue. The small palladium and cadmium pieces are glued above, so that all three elements are arranged in segments of 120°

time. Presently a voltage of 2850 V is applied to the formation chamber and conducted to the aluminum disc by the ball bearing. Fig. 4.8 illustrates how the aluminum disc is connected to the formation chamber. In oder to improve the ion beam quality and the starting conditions of the ions, the alignement of the pellet holder was modified. Here, the axis of the aluminum disc and hence, the axis of the sample was shifted by 3 mm out of the ion optics axis. In this configuration the target material can be changed with no realignment of the laser path. This allows also to produce the ions directly in the ion optics axis and hence, to eject the ions into the ion optics without any deflection. Fig. 4.9 a) shows the principle. The laser hits the sample on a circle around the pellet axis with a radius of 3 mm. Fig. 4.9 b) shows a drawing of the new holder.

4.2.3 The Ion Optics and its Modifications

The Configuration of the Ion Optics

The ion optics of the ISOLTRAP laser ion source consists of several elements, as shown in fig. 4.11. The plasma is generated by material ablation from a probe pellet using a high energetic laser pulse. In order to generate an undisturbed plasma plume, the plasma region is surrounded by the so-called formation chamber, which is held at the same potential as the aluminum disc hosting the target probe, since both are connected by the ball-bearing. The voltage of 2850 V applied to the formation chamber defines the initial potential of the ion bunch, which is the same as the initial potential of the ions coming from the ISOLTRAP cooler and buncher. Next, the ions are extracted into the ion beam line by the extraction electrode, which is put on a negative potential of -1100 V. The einzel lens at $0 - 1100 - 0$ V and the steerer at 1940 V focus and guide the

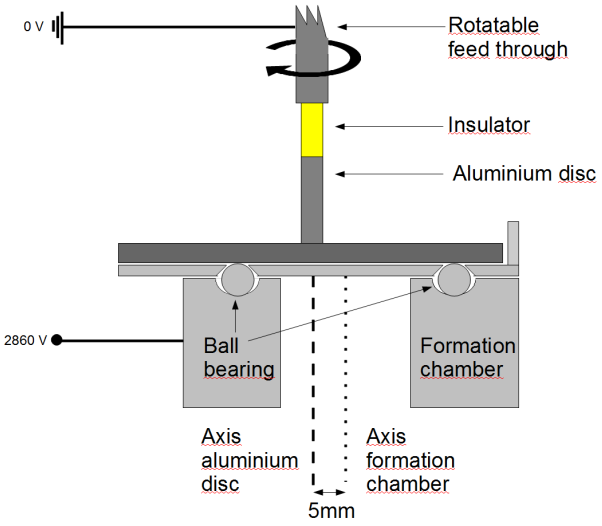

Figure 4.8: An illustration, how the aluminum disc is connected conductively to the formation chamber by a ball bearing. The axis of the alumium disc and the formation chamber are shifted by 5 mm and the aluminum disc is separated to the rotatable feed through by an insulator. Presently a voltage of 2860 V is applied to the aluminum disc. The dimensions are not to scale.

ions into the quadrupole deflectors, which bent them by 90° and guide them into the main ISOLTRAP beam line, towards the preparation trap. Tab. 4.2 shows an overview of the electrode potentials.

Table 4.2: An overview over the voltages presently applied to the different elements of the laser ablation ion optics.

Electrode	**Voltage / V**
Formation chamber	2,860
Extraction electrode	-1,800
Lens	1,700
Steerer	1,940
Quadrupole deflector 1	3,782
Quadrupole deflector 2	2,885
Quadrupole deflector 3	1,425
Quadrupole deflector 4	2,652

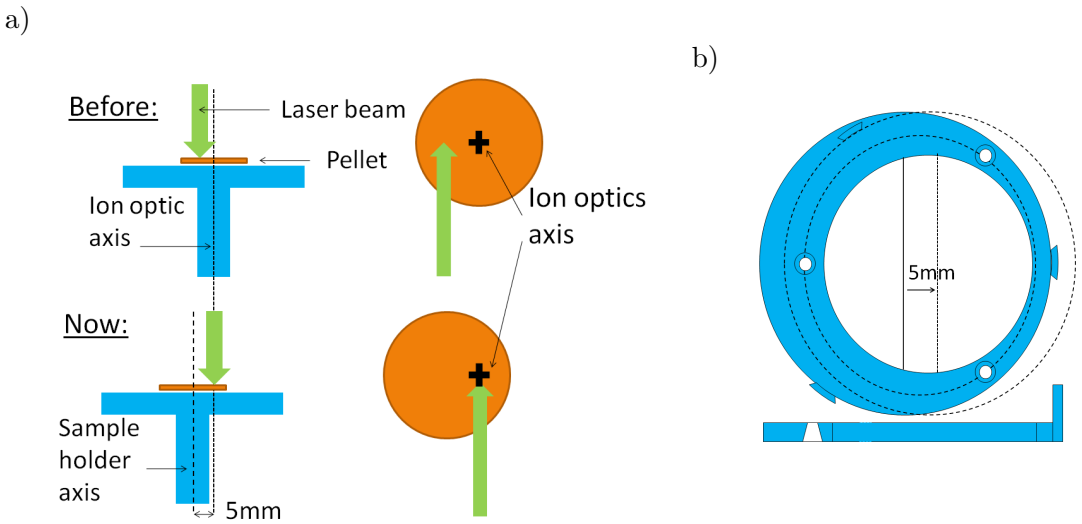

Figure 4.9: a)The drawing illustrates the modifications to the sample holder. Before, the ion optics axis and the axis of the aluminum disc were at the same position, while the laser spot was off axis. Thus, the ions were also produced off axis. Now, the ion optics axis and the laser spot on the pellet are at the same position, while the center of the aluminum disc is brought off the axis by 5 mm. As a result, the ions are injected into the ion optics with less deflections in the horizontal direction. b) A drawing of the new holder of the aluminum disc. Here, the small holes show the positions of the balls of the ball bearing. The inner hole is shifted by 5 mm compared to the symmetry axis of the alumium disc. The dashed lines represent the old geometry of the holder, where the center of the hole and hence, the center of the aluminum disc was identical with the axis of the ion optics. The dimensions are not to scale.

Recent Modifications and Simulations with SIMION©

New geometries of the formation chamber and the extraction electrode were simulated and tested in order to improve the ion production stability and the emittance of the ion beam. The simulations were performed with the SIMION© software, which is able to calculate the electric fields of a given electrode configuration with defined applied voltages by solving the Laplace equation and hence, the ion trajectories in those fields. The simulations have shown that several parameters play an important role in the transport efficiency and beam quality. Most crucial are: The length of the formation chamber, the diameter of the opening in the extraction electrode, the geometry of the extraction electrode, the distances between the different optical elements, and the ion starting conditions, such as the initial kinetic energy and the position. Several lengths of the formation chamber and a different geometry of the extraction electrode, the Pierce geometry [Pie49], which improves the emittance of the particle, were tested and simulated. Fig. 4.10 shows the simulated ion trajectories for different formation chamber lengths.

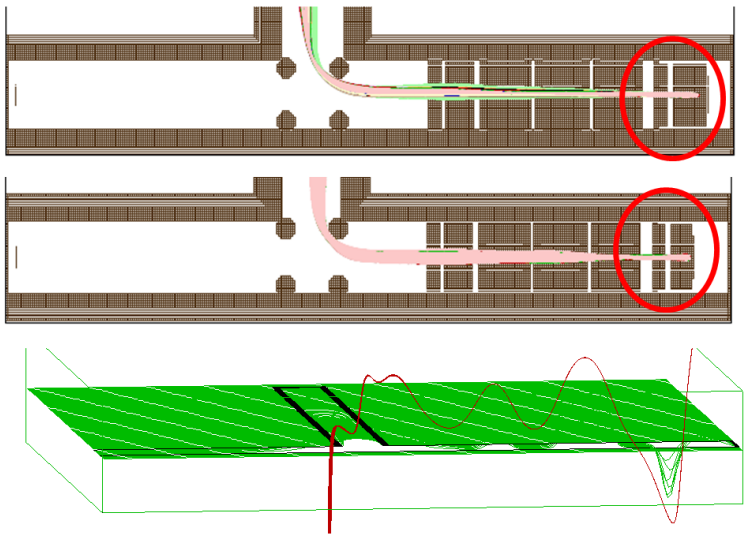

Figure 4.10: Ion trajectory simulations for two different formation chamber lengths (red circuled). As a result, the ion trajectories differ after the quadrupole deflector. The graph below shows the corresponding potential energy of the ions at the different elements for the second simulation with shorter formation chamber.

The unknown factor is the energy distribution in the plasma plume, defining the starting conditions of the ions. Therefore, the starting conditions were approximated to the scenario described in chapter 4.1 by a Gaussian velocity distribution and also by a conoidal velocity distribution. Since several parameters, such as the temperature and the dimensions of the plume were unknown and small changes in those parameters led to large differences in the results, only the qualitative effects of the different elements could be studied. First of all, the advantages of a perpendicular kinetic starting energy of the ions and the production of ions in the ion optics beam line could be obtained and hence, the laser beam and the ion optic was modified as described in section 4.2.2. Later, off-line experiments with the real setup were performed in which a new shorter formation chamber with only 20 cm tube length and two different extraction electrodes with Pierce geometry were tested. Unfortunately, it was not easy to compare the results since the ion transfer is very sensitive to small changes of the alignment of the ion optics. Because it seemed that the Pierce geometry didn't give a large advantage, the present setup consists for reasons of simplification of the long formation chamber and the extraction electrode without Pierce geometry. Future tests should decide which geometry is really best for an optimal emittance and provides the highest ion production stability.

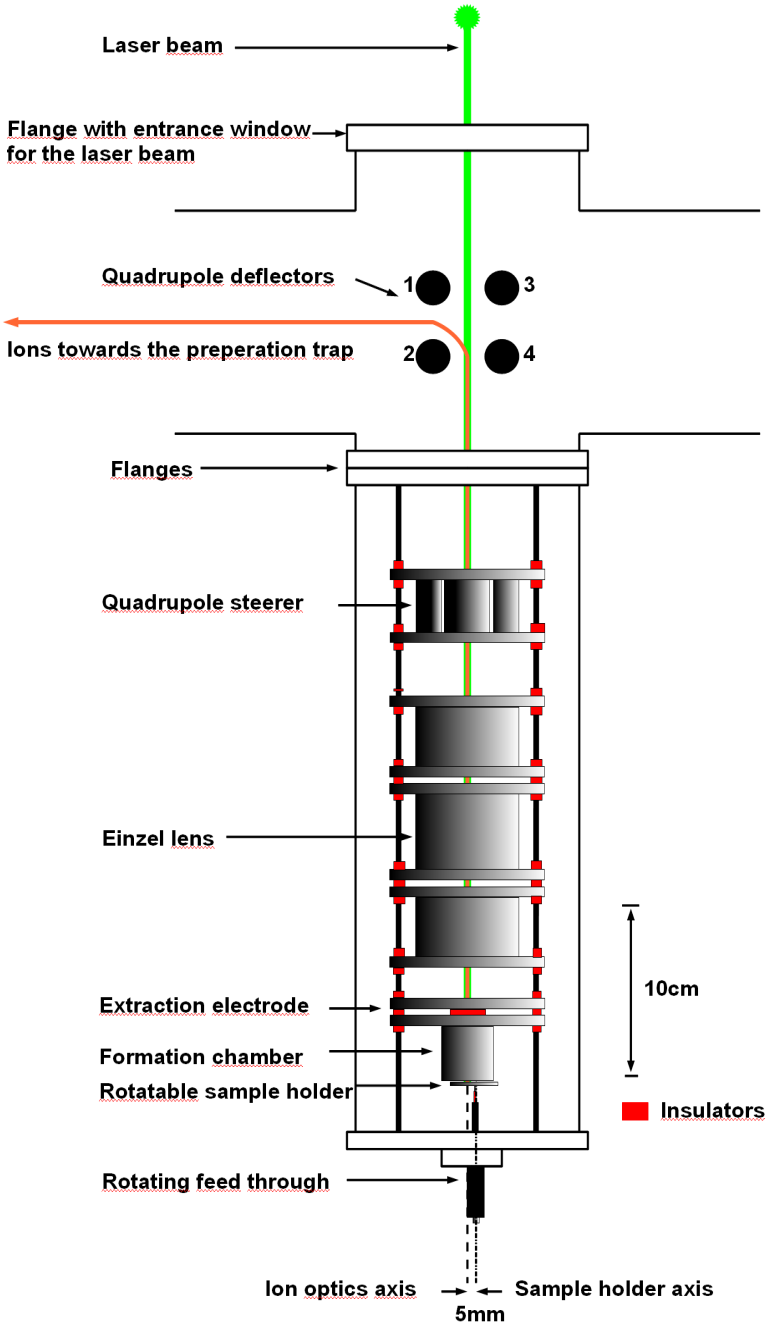

Figure 4.11: The present setup of the ion optics of the laser ablation ion source at ISOLTRAP. All ion optics elements, such as the sample holder, the formation chamber, the einzel lens, the quadrupole steerer and the quadrupole deflectors are shown. Furthermore, the lateral off-set between the aluminum disc of the sample holder and the ion optics axis is shown.

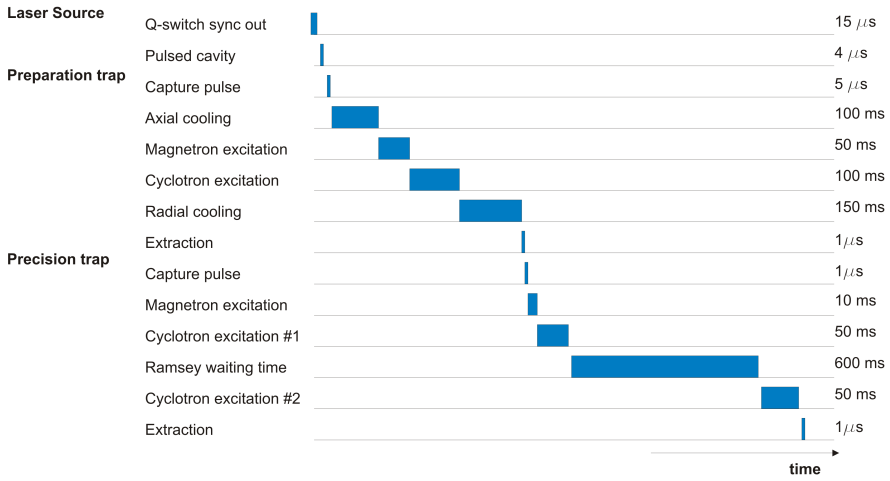

Figure 4.12: The timing sequence of a (50-600-50) ms Ramsey excitation of $^{110}Pd^{+}$. The measurement cycle is triggered by the Q-switch synchronization output signal of the laser. All following steps are synchronized in order to guide and manipulate efficiently the ions through the ISOLTRAP setup. The lengths of the time windows are not to scale.

4.3 Ion Production Spectrum of the ISOLTRAP Laser Ion Source

Presently, the ion species produced the laser ablation ion source at ISOLTRAP are the stable isotopes of cadmium, palladium, and the clusters of ^{12}C. In the following, the ion selection and excitation process from the source to the precision trap is given on the example of the palladium isotope $^{110}Pd^{+}$, followed by a summary of the production of cadmium and carbon cluster ions.

4.3.1 Ion Production, Selection, and Excitation of $^{110}Pd^{+}$ and $^{110}Cd^{+}$

In the following example, laser pulses of about 17 mJ were shot on the palladium segment in order to produce a stable and sufficient number of palladium ions. This energy corresponds (see eq. (4.7)) to an laser power density of $\rho = 9.4(5) \cdot 10^7\,\mathrm{W/cm^2}$, to be compared to the ablation threshold, where the Pd ions start to appear, of about $\rho = 8.7(4) \cdot 10^7\,\mathrm{W/cm^2}$. The number of created ions can be increased by raising the laser power density. The dependence seems to be linear with no saturation observed up to the maximum laser energy. In the present experiments, the laser pulse energy was used to regulate the number of ions in the system. The measurement timing sequence of a (50-600-50) ms Ramsey excitation [Geo07]4 of $^{110}Pd^{+}$ shown in fig. 4.12 is representative for all measurements regarded in this thesis. Fig. 4.13 shows a time-of-flight spectrum of all extracted ions in front of the preparation trap. Here, the ions were detected by a micro-channel plate (MCP2). The peak around 33.5 μs corresponds to the ablated stable

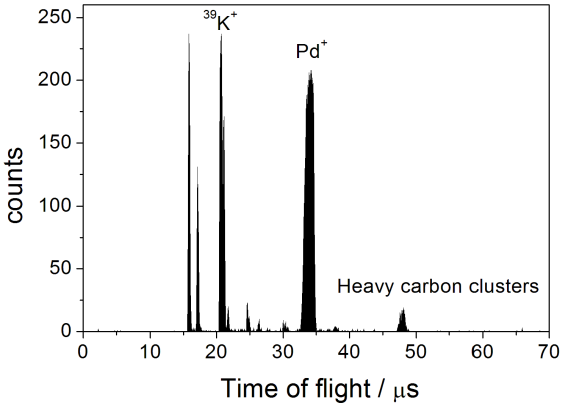

Figure 4.13: A time of flight spectrum of the ablated particles from the palladium segment. The strong peak from 32.8 μs to 34.9 μs are the ablated stable palladium isotopes $^{102}Pd^+$, $^{104}Pd^+$, $^{105}Pd^+$, $^{106}Pd^+$, $^{108}Pd^+$, and $^{110}Pd^+$. Furthermore, a contamination of the spectrum with heavy carbon clusters such as $^{12}C^+_{17,18,19}$ and $^{39}K^+$ was observed.

palladium ions $^{102}Pd^+$ (1.02 % natural abundance), $^{104}Pd^+$ (11.14 %), $^{105}Pd^+$ (22.23 %), $^{106}Pd^+$ (27.33 %), $^{108}Pd^+$ (26.46 %), and $^{110}Pd^+$ (11.72 %), while the remaining signals represent contaminations of the pellet such as the heavy carbon clusters $^{12}C^+_{17,18,19}$ and $^{39}K^+$. Contaminations occur due to impurities of the material or due to the preparation process of the pellet, for example from glue, fingerprints or air contact and can be removed by the right timing of the capture pulse or by the buffer gas purification in the preparation trap. $^{110}Pd^+$ is separated from the other isotopes in the preparation trap (see chapter 3.2.2). Fig. 4.14 a) shows a so-called cooling resonance for $^{110}Pd^+$, where the number of ions passing the diaphragm is registered as a function of the applied frequency around ω_c. The peak width and position allow reaching a resolving power of 20000. The effect of the cleaning and cooling in the preparation trap is shown in fig. 4.14 b). Here, the black line represents the spectrum in the preparation trap without any excitations. The stable palladium ions and several contaminations are able to pass the diaphragm in the endcap of the preparation trap and a broad peak at 51 μs is obtained which contains all stable Pd isotopes. When the buffer gas cleaning procedure is applied, only $^{110}Pd^+$ can pass the diaphragm. The peak with the black fill at 52.0 μs shows the cleaned spectrum, which contains only $^{110}Pd^+$. Next, the cleaned and cooled bunch of $^{110}Pd^+$ is guided into the precision trap, where the cyclotron frequency is determined. A time of flight resonance of the Ramsey type of $^{110}Pd^+$ is shown in fig. 4.15. Here, the cyclotron excitation scheme was 50 ms of quadrupolar excitation, 600 ms of waiting time, and a second quadrupolar excitation of 50 ms and the cyclotron frequency was measured to $\nu_c = 8264448.496\,(6)$ Hz. The ion production and excitation process of cadmium is similar to the palladium production. Due to the different pellet position,

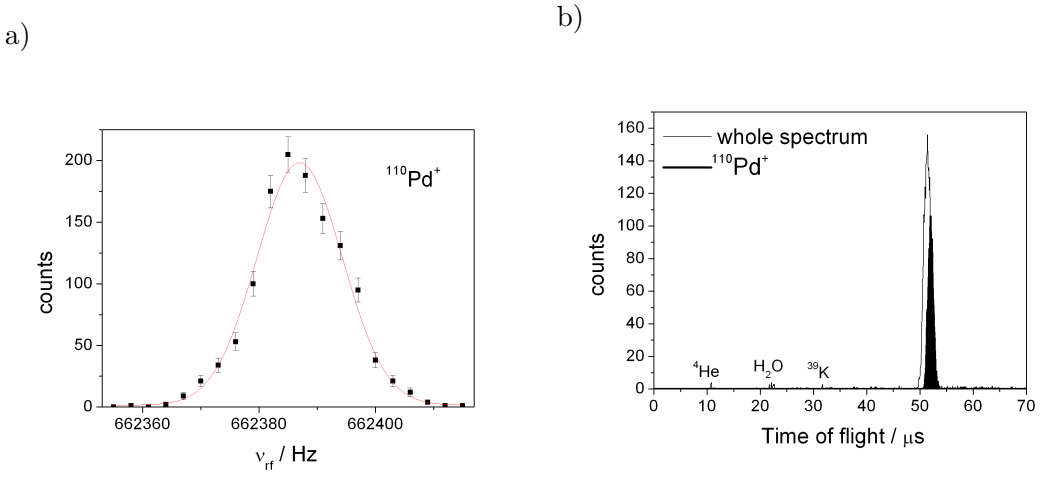

Figure 4.14: a) A scan around ω_c of $^{110}Pd^+$ in the preparation trap with an excitation time of $T_{rf} = 100\,\text{ms}$. The line is a Gaussian fit to the data. A center frequency of $\nu_{rf} = 662386.9\,(3)\,\text{Hz}$ with a FWHM of $34.5\,(8)\,\text{Hz}$ was obtained resulting in a mass resolving power of $m/\Delta m = 2 \cdot 10^4$. b) The ToF spectrum of the palladium pellet behind the preparation trap. Here the black line represents the spectrum without any excitation. All stable palladium isotopes as well as minor contaminations are visible. The line with the black fill represents the cleaned peak of $^{110}Pd^+$ after magnetron and cyclotron excitation. No contaminations or other palladium isotopes are observed any more.

the timing sequence and the applied voltages are slightly different. On average, the laser pulse energy was about 11.2 mJ, which corresponds to a laser power density of $6.2(3)\cdot 10^7\,\text{W/cm}^2$. Fig. 4.16 shows a $(30 - 840 - 30)\,\text{ms}$ Ramsey time-of-flight resonance of $^{110}Cd^+$.

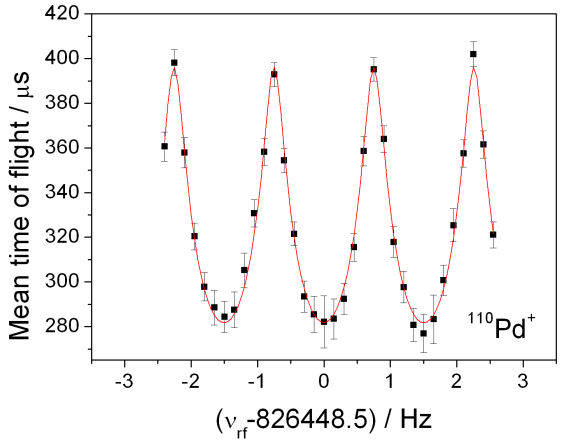

Figure 4.15: A $(50 - 600 - 50)$ ms Ramsey excitation resonance of $^{110}Pd^{+}$. About 1300 ions were recorded. The solid line shows the corresponding fit to the data [Kre07]. The error bars to the data points include the width of the time-of-flight distribution of the ions at the corresponding frequency as well as the statistical uncertainty.

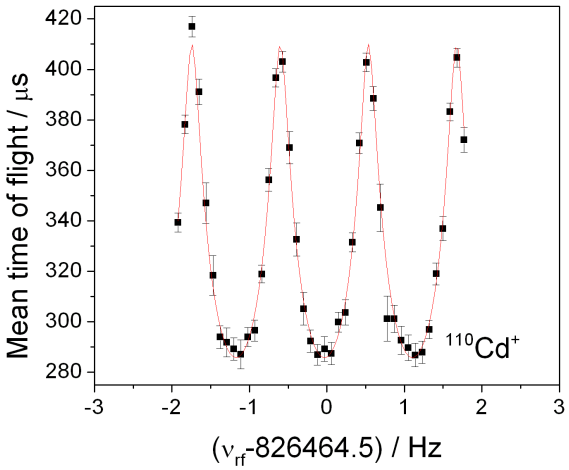

Figure 4.16: A $(30 - 840 - 30)$ ms Ramsey excitation scheme of $^{110}Cd^{+}$. About 3600 ions were recorded. The solid line shows the corresponding fit to the data [Kre07].

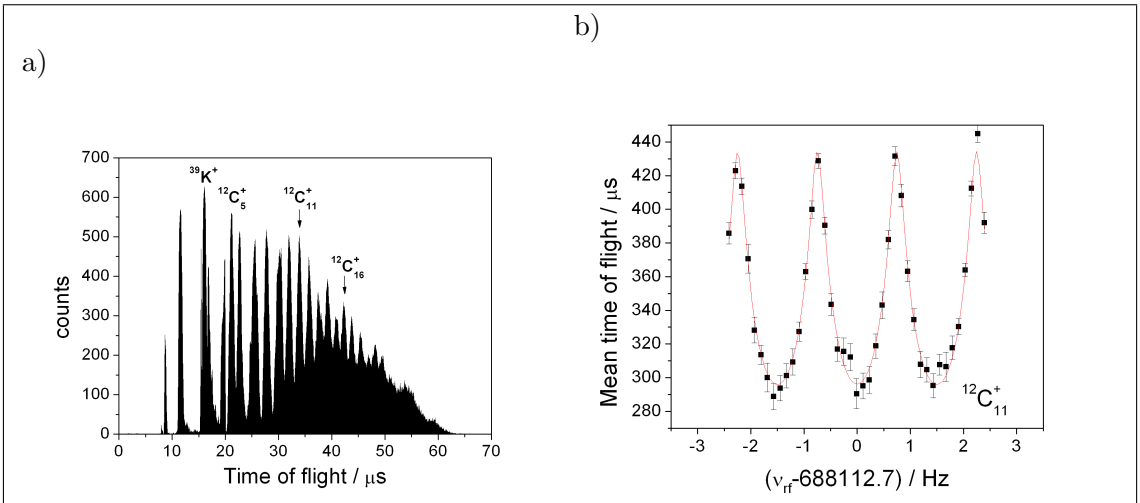

Figure 4.17: a) The carbon cluster mass spectrum, recorded in front of the preparation Penning trap. The laser power density on the SIGRADUR© pellet was $4.6(2) \cdot 10^7\,\mathrm{W/cm^2}$. The strong lines in the middle represent clusters of $^{12}C_n$. In total, carbon clusters from $n = 3$ to $n = 24$ could be observed with the ISOLTRAP laser ion source. b) A $(50 - 600 - 50)$ ms Ramsey excitation resonance of $^{12}C_{11}^+$. About 1900 ions were recorded. The solid line shows the corresponding fit to the data [Kre07].

4.3.2 Carbon Cluster Production and Excitation

The carbon clusters, ablated from the SIGRADUR© pellet cover a wide mass range as shown in fig. 4.17 a). Here, the time-of-flight spectrum was recorded in front of the preparation trap and $^{12}C_n$ clusters from $n = 3$ ($m = 36\,\mathrm{u}$) and $n = 24$ ($m = 288\,\mathrm{u}$) could be identified [Böh09]. In general, a strong dependency of the relative production of different clusters on the laser energy could be observed and clusters were obtained from 2 mJ ($\rho = 1.1 \cdot 10^7\,\mathrm{W/cm^2}$) to about 9 mJ ($\rho = 4.95 \cdot 10^7\,\mathrm{W/cm^2}$), whereas the highest and most stable production rate was observed for around 8 mJ ($\rho = 4.6 \cdot 10^7\,\mathrm{W/cm^2}$), as used for the examples in fig. 4.17 a) and fig. 4.17b). Here, a time-of-flight resonance with a $(50 - 600 - 50)$ ms Ramsey excitation of $^{12}C_{11}^+$ is shown.

5 Q-Value and Mass Measurements of the ^{110}Pd and ^{110}Cd Mass Doublet

The ^{110}Pd to ^{110}Cd mass doublet is one of the eleven possible candidates for neutrinoless double beta decay, with Q-values higher than 2000 keV (see tab. 1.1), which have strongly lowered half-lives (see chaper 2.2.1). This makes it an interesting candidate for future experiments, which search for a $(0\nu\beta\beta)$-decay signal. A high-precision Q-value measurement of this transition with an uncertainty below 1 keV is of outmost importance in experiments with these $(0\nu\beta\beta)$-candidates to identify the sharp peak of the $(0\nu\beta\beta)$-decay in the total $\beta\beta$-spectrum, as illustrated in fig. 2.5. The Q-value of the ^{110}Pd/^{110}Cd transition was measured at ISOLTRAP within this thesis. Here, the ions were created by laser ablation using the laser ablation ion source, described in the previous chapter and brought towards the double Penning trap system. Both ^{110}Pd and ^{110}Cd were studied alternately over a longer period and in total over 100 frequency measurements of ^{110}Pd and ^{110}Cd were performed. Furthermore, the masses of ^{110}Pd and ^{110}Cd were determined using for the first time carbon clusters at ISOLTRAP as mass references for a non-carbon species. In the following, a description of the Q-value, and mass measurement evaluation process is given, followed by the results and their discussions.

5.1 Mass and Q-Value Measurements

5.1.1 Determining Masses and Q-Values in Penning Traps

The mass and Q-value measurements in Penning traps are based on the determination of the cyclotron frequency $\nu_c = \omega_c/(2\pi) = qB/(2\pi m)$. While the cyclotron frequency ν_c can be measured precisely, the magnetic field has to be well calibrated in order to extract the mass. For this purpose, a reference ion with a very well-known mass (m_{ref}) is studied within a short time period to minimize the effect of the magnetic field drifts. This leads to the following formula for the mass of interest:

$$m = \frac{\nu_{c,ref}}{\nu_c} \cdot (m_{ref} - m_e) + m_e = r \cdot (m_{ref} - m_e) + m_e \quad , \tag{5.1}$$

where m_e is the electron mass and r is the ratio of the cyclotron frequency ν_c of the ion of interest and the cyclotron frequency $\nu_{c,ref}$ of the reference ion.

At the same time, the Q-value of the decay between a mother nucleus with mass m_m

and a daughter nucleus with mass m_d is given by the mass difference of both nuclei:

$$Q = (m_m - m_d) = \left(\frac{\nu_{c,d}}{\nu_{c,m}} - 1\right)(m_d - m_e) = (r-1)(m_d - m_e)\ , \tag{5.2}$$

where $\nu_{c,d}$ is the cyclotron frequency of the daughter nucleus, $\nu_{c,m}$ the cyclotron frequency of the mother nucleus, and r is the ratio of the cyclotron frequencies. As will be shown later in the description of the Q-value determination there is no need for a very well-known reference mass in Q-value determination.

Cyclotron Frequency-Ratio Determination

The magnetic field of the Penning trap drifts in time [Kel03]. Several phenomena lead to a long term decrease of the magnetic field magnitude and superposed random short time fluctuations, as described later in this chapter. There are several ways to correct the magnetic field drifts in determining the cyclotron frequency ratio. The two methods, the so-called "interpolation" method and the so-called "polynomial" method, which were used to determine the masses and the Q-value of ^{110}Pd and ^{110}Cd, are described below. In the following, ion 1 stands for the mother nuclide (ion of interest), ion 2 stands for the daughter nuclide (reference ion) in Q-value (mass) measurements, and $\nu \equiv \nu_c$ for the cyclotron frequency for the sake of simplicity.

1. **Interpolation method:** At ISOLTRAP, the interpolation method is used conventionally for mass measurements. The frequency of ion 2 is measured "sandwich-wise" just before and after ion 1. In the evaluation, the frequency of ion 1 is linearly interpolated to the time, when ion 2 was measured to compensate the magnetic field fluctuations. The interpolation is a weighted average to the short fluctuations and it takes in addition the long term fluctuations into account. Fig. 5.1 a) illustrates the principle. The interpolated cyclotron frequency of ion 2 can be calculated as

$$\nu_2(t_1) = t_1 \cdot \frac{\nu(t_2) - \nu(t_0)}{t_2 - t_0} + \frac{t_2 \cdot \nu(t_0) - t_0 \cdot \nu(t_2)}{t_2 - t_0}\,, \tag{5.3}$$

   where t_1 is the time when ion 1 was measured, t_0 and t_2 the times when ν of ion 2 was studied, and $\nu(t_0)$ and $\nu(t_2)$ the cyclotron frequencies of the two measurements of the ion 2. For convenience we assume $t_0 = 0$ and obtain

$$\nu_2(t_1) = \frac{t_1 \cdot [\nu(t_2) - \nu(t_0)] + t_2 \cdot \nu(t_0)}{t_2}\,. \tag{5.4}$$

   Then, the frequency ratio of a single measurement is calculated by

$$r^n = \frac{\nu_2^n}{\nu_1^n}\,, \tag{5.5}$$

   where n refers to the number of a measurement in a whole data set.

2. **Polynomial method:** Here, the basic idea is to approximate the time depen-

dency of the cyclotron frequency over several measurements by a fit function. The frequency ratio is a fit parameter of this function. This method is illustrated in fig. 5.1 b) and already used in a similar way at other experiments. The cyclotron frequencies of the two ions $\nu_1(t)$ and $\nu_2(t)$ are functions of time due to the time dependency of the magnetic field $B(t)$. Approximating the magnetic field behavior by a polynomial of third degree leads to

$$B(t) = B_0 \cdot \left(a + b \cdot t + c \cdot t^2 + d \cdot t^3\right) , \tag{5.6}$$

where B_0 is the magnitude of the magnetic field when the first measurement starts and a, b, c, and d are the coefficients of the polynomial. Then, the cyclotron frequencies can be written as functions of time by

$$\nu_i(t) = \frac{q}{2\pi m_i} B(t) \quad \text{with} \quad i = 1, 2 . \tag{5.7}$$

Both frequencies can be connected by the frequency ratio $r = \frac{\nu_2}{\nu_1}$ to

$$\begin{aligned} \nu_1(t) &= r \cdot \nu_2(t) && (5.8)\\ &= r \cdot \underbrace{\frac{q}{2\pi m_1} B_0}_{const.} \cdot \left(a + b \cdot t + c \cdot t^2 + d \cdot t^3\right) \quad \text{and} && (5.9)\\ \nu_2(t) &= \underbrace{\frac{q}{2\pi m_1} B_0}_{const.} \cdot \left(a + b \cdot t + c \cdot t^2 + d \cdot t^3\right) . && (5.10) \end{aligned}$$

Multiplying the constant $qB_0/(2\pi m)$ to the fit parameters a, b, c, and d leads to the fit functions

$$\nu_1(t) = (A + B \cdot t + C \cdot t^2 + D \cdot t^3) \cdot r \tag{5.11}$$

and

$$\nu_2(t) = A + B \cdot t + C \cdot t^2 + D \cdot t^3 , \tag{5.12}$$

where A, B, C, D, and the cyclotron frequency r are the fit parameters. In the final procedure, the two fit functions are fitted simultaneously to the two data sets of the two ions, with common fit parameters A, B, C and D.

5.1.2 Uncertainties in Frequency and Frequency-Ratio Determination

Several uncertainties have to be considered for the frequency and frequency-ratio measurements at ISOLTRAP. In 2002-2003, an extensive study using carbon clusters was performed to determine the sources of the error [Bla03, Kel03]. The origin of the errors are of statistical and systematic nature. The most important ones regarding the frequency and the frequency-ratio determination are listed below.

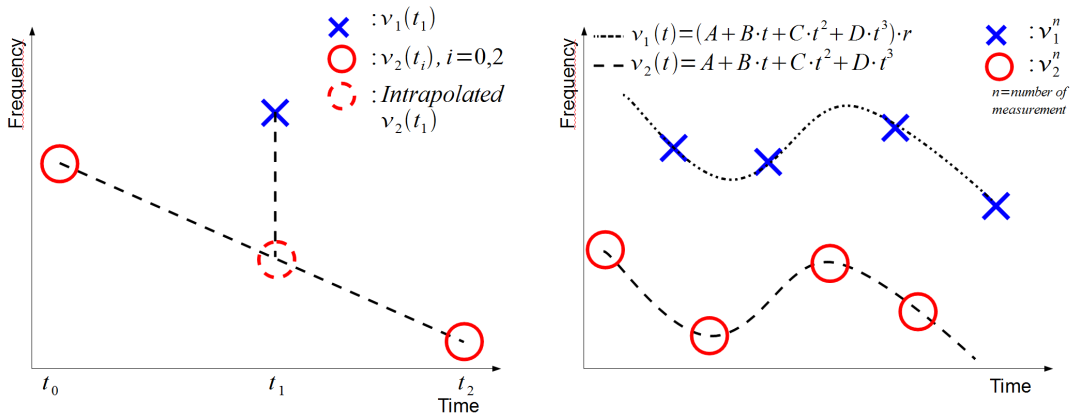

Figure 5.1: Two methods for determining cyclotron frequency ratios in Penning trap mass measurements. a) In the interpolation method, the frequencies of ion 2 are interpolated to the time when ion 1 was studied in order to compensate the drift and the fluctuations of the magnetic field. b) In the polynomial method, the ratio is determined by two polynomials, which are fitted to the two data sets with common fit parameters A, B, C and D. The polynomials follow the behavior of the cyclotron frequency with time and are proportional to the drift and fluctuations of the magnetic field. The cyclotron frequency ratio r as a fit parameter. (ν_1 does not have to be necessarily higher than ν_2. The procedures are also valid for $\nu_2 > \nu_1$)

Uncertainties in Frequency Determination

1. **Statistical uncertainty:** The statistical uncertainty of the cyclotron frequency depends on the total number N_{tot} of ions recorded and the quadrupole excitation time T_q. An empirical formula for the relative standard deviation was found [Bol01] to be

$$\frac{s(\nu)}{\nu} = \frac{c}{\sqrt{N_{tot}}T_q}, \tag{5.13}$$

where the constant c was determined to be $c = 0.898\,(8)$ [Kel03]. As shown above, the statistical error decreases with the number of ions and the excitation time. This uncertainty is provided by the fitting program. Typical values obtained by the Ramsey method as described in chapter 3.1.3 within this thesis are of the order of $s(\nu)/\nu \approx 5 \cdot 10^{-9}$.

2. **Magnetic field drifts:** Several reasons lead to a variation in time of the magnetic field magnitude in the precision Penning trap, which influences the cyclotron frequency directly (see eq. (3.1)). The magnetic field decreases logarithmically [Ket99], due to a steady decrease of the current in the superconducting

coils of the magnet, called the flux-creep phenomenon [And62, And64]. For short time intervals (up to years), the decrease of the magnetic field can be approximated by a linear decrease [Kel03]. If ferromagnetic or paramagnetic materials are brought close to the magnet, they get magnetized and hence, remove energy from the magnet. This can cause field jumps of the order of up to 10^{-7} [Kel03] for large metallic objects, such as the ISOLDE hall crane. Furthermore, fluctuations in the magnetic field can be caused by the temperature fluctuations in the liquid helium level due to pressure fluctuations of the helium recovery line [VD92]. Also the temperature fluctuations in the hall influence the temperature dependent magnetic permeability of the materials inside the magnetic bore, which surround the precision Penning trap. In total, the magnetic field undergoes a slow decrease, which is imposed by random short time fluctuations. The long-term linear decrease at ISOLTRAP was determined by systematic studies [Kel03] to be[1]

$$\frac{\delta B}{\delta t}\frac{1}{B} = -2.30\,(3) \times 10^{-9}/h\,. \tag{5.14}$$

The random short time fluctuations cause an additional uncertainty to the interpolation of the cyclotron frequency reference ions (see eq. (5.4)) in the interpolation method, which was determined [Kel03] to a relative uncertainty of

$$\frac{u_B}{\nu} = 6.35\,(45) \cdot 10^{-11} \cdot \Delta T/min\,, \tag{5.15}$$

where ΔT is the time between the first and the second measurement of the reference ion. These short time fluctuations are the reason why the measurements of the reference ion should be as close in time as possible to each other. At the same time one has to consider that the standard uncertainty of the frequency measurement depends on the total number of ions measured and on the measurement time as shown in eq. (5.13). Therefore, during the Q-value studies a typical frequency measurement took about 15 min.

3. **Contaminations:** Contamination with isobars and even isomers have to be considered because the applied cleaning procedure might not be fully efficient. Their presence leads to small frequency shifts, which are linearly proportional to the number of contaminant ions [Kön95, Bol92]. Reducing the number of ions in the trap reduces the effect. In addition, one can correct the shift by the countrate analysis, where the real cyclotron frequency for a single ion in the trap can be extrapolated [Kel03].

Uncertainties in the Frequency-Ratio Determinations

1. **Mass-dependent systematic effect:** A mass-dependent frequency ratio shift can occur due to imperfections of the electrostatic quadrupole field and due to

[1] In [Kel03] the value was given due to a type error by $\frac{\delta B}{\delta t}\frac{1}{B} = -2.30\,(3) \times 10^{-8}/h$. The corrected actual measured value is given in eq.(5.14)

misalignments of the electrostatic trapping fields with respect to the magnetic field axis [Bro86, Bol96]. Here, the relative standard uncertainty of the frequency ratio r was determined at ISOLTRAP [Kel03] to

$$\frac{u_m}{r} = 1.6 \cdot 10^{-10} \cdot (m_1 - m_2)/u\,. \tag{5.16}$$

This error is marginal compared to other uncertainties if $\Delta m = m_1 - m_2 \approx 0$, which is the case for Q-value measurements. Furthermore, eq. (5.16) shows the importance for mass measurements with a small difference between the mass of the ion of interest and the mass of the reference ion.

2. **Residual systematic uncertainties:** In addition to the mass-dependent frequency-ratio shift, a relative residual systematic uncertainty was observed at ISOLTRAP [Kel03], which is of the order of

$$\frac{u_{res}}{r} = 8.9 \cdot 10^{-9}\,. \tag{5.17}$$

In many recent studies at ISOLTRAP this uncertainty is an upper limit for the mass accuracy of the ISOLTRAP experiment. However, this uncertainty was obtained as a fit to carbon clusters with various masses and hence shows a global effect [Kel03]. If $\Delta m \approx 0$, as in the case of Q-value measurements, one can assume that this uncertainty is much lower than that of eq. (5.17) and it can be neglected.

5.1.3 Evaluation Procedure for Mass and Q-Value Measurements

In the following, the evaluation procedure for mass and Q-value measurements is presented. Here, one has to distinguish the interpolation method and the polynomial method to determine the frequency ratio discussed in section 5.1.1. The different influences of the uncertainties mentioned above to the frequency and frequency ratio are discussed.

Individual Cyclotron Frequencies

1. **Interpolation method:** To determine the individual cyclotron frequency of each measurement one has to distinguish between ion 1 and ion 2. The standard uncertainty in ν of ion 1 is simply given by eq. (5.13) and can be obtained from the fitting program. In case of ion 2, the standard deviation of the interpolated cyclotron frequency of the measurement n can be derived from eq. (5.4) and is given by

$$s\left(\nu_2^n\right)(t_1) = \sqrt{\left[\frac{t_1}{t_2}s_2\right]^2 + \left[\left(1 - \frac{t_1}{t_2}\right)s_0\right]^2}\,, \tag{5.18}$$

where ν_k is a shortcut for $\nu_2^i(t_k)$ and s_k for $s(\nu_2^i)(t_k)$. In addition, the uncertainty due to the magnetic field fluctuations u_B/r given by eq. (5.15) has to be taken into account and a propagation of the uncertainty leads to a relative uncertainty

of ion 2 of

$$\frac{u_c}{\nu_2^n} = \sqrt{\left[\frac{s\left(\nu_2^n\right)}{\nu_2^n}\right]^2 + \left[\frac{u_B\left(\nu_2^n\right)}{\nu_2^n}\right]^2}\,. \tag{5.19}$$

2. **Polynomial method:** Here, only the statistical uncertainty (eq. (5.13)) obtained by the fitting program is considered. The magnetic field drifts are taken into account by the polynomials.

Cyclotron Frequency Ratio

The final uncertainty in r based on a set of measurements of ν_1 and ν_2 depends on the method used to determine the frequency ratio.

1. **Interpolation method:** With this method, the uncertainty of the cyclotron frequency ratio of one measurement $r^n = \nu_2^n/\nu^n$ combines the frequency uncertainty of ion 1 and ion 2. A propagation of the error leads to the relative standard uncertainty of the cyclotron frequency ratio:

$$\frac{u_c(r^n)}{r^n} = \sqrt{\left[\frac{s(\nu_1^n)}{\nu_1^n}\right]^2 + \left[\frac{u_c(\nu_2^n)}{\nu_2^n}\right]^2}\,. \tag{5.20}$$

   If several measurements are performed, the final cyclotron frequency ratio is given by the weighted average r of the single frequency ratios r^n (see eq. (5.5):

$$r = \frac{\sum\limits_i \frac{r^n}{u_c^2(r^n)}}{\sum\limits_n \frac{1}{u_c^2(r^n)}}\,. \tag{5.21}$$

   where the relative standard uncertainty is calculated by

$$\frac{u_{int}(r)}{r} = \frac{1}{r\sqrt{\sum\limits_n \frac{1}{u_c^2(r^n)}}}\,. \tag{5.22}$$

2. **Polynomial method:** When this method is used, the cyclotron frequency ratio r is a fit parameter. Then, its relative standard uncertainty is given by the fitting program (based on the χ^2 minimization procedure):

$$\frac{u_{pol}(r)}{r} = \frac{s(r)}{r}\,. \tag{5.23}$$

   Typically, relative uncertainties of about $3 \cdot 10^{-9}$ were obtained with this method.

In case of Q-value measurements of isobars, only the relative standard uncertainty $u(r)/r$ derived above using one of the described methods (eq. 5.22) or eq. (5.23) has to be taken

into account, since the mass-dependent systematic effect u_m/r (eq. (5.16)) and the residual systematic uncertainty u_{res}/r (eq. (5.17)) disappear for $\Delta m \approx 0$ as described in chapter 5.1.2. In the case of mass measurements, the mass difference between the ion of interest and the reference ion cannot be neglected in general and the mass-dependent systematic effect and the residual systematic uncertainty have to be taken into account. Then, the total relative uncertainty of the ratio is given by

$$\frac{u_{tot}(r)}{r} = \sqrt{\left[\frac{u(r)}{r}\right]^2 + \left[\frac{u_m}{r}\right]^2 + \left[\frac{u_{res}}{r}\right]^2} \quad . \tag{5.24}$$

Mass Evaluation

The uncertainty of the mass of the ion of interest is obtained by an error propagation of the mass formula (eq. (5.1)):

$$u(m) = \sqrt{[\underbrace{(m_{ref} - m_e)}_{\approx m_{ref}} \cdot u(r)^2 + [r \cdot u(m_{ref})]^2 + [\underbrace{(1-r) \cdot u(m_e)}_{\approx 0}]^2} \,. \tag{5.25}$$

Here, the mass of the electron and its error are several magnitudes smaller than the mass and mass uncertainty of the reference ion and can be neglected. This leads to

$$u(m) = \sqrt{[m_{ref} \cdot u(r)]^2 + [r \cdot u(m_{ref})]^2} \,. \tag{5.26}$$

Q-Value Evaluation

An error propagation of eq. (5.2) leads to the uncertainty of the Q-value.

$$u(Q) = \sqrt{[\underbrace{(m_d - m_e)}_{\approx m_d} \cdot u(r)]^2 + [\underbrace{(r-1)}_{\approx 0} \cdot u(m_d)]^2 + [\underbrace{(1-r) \cdot u(m_e)}_{\approx 0}]^2} \quad . \tag{5.27}$$

The mass of the electron and its error can be neglected as for the mass evaluation. Additionally, the term $(r-1)$ is usually very close to 0 since mother and daughter nucleus are close in mass in most cases, which makes the contribution of $u(m_d)$ almost negligible (e.q. for ^{110}Pd/^{110}Cd it would be around $0.02 \cdot u(m_d) \approx 60\,\text{eV}$). This can be demonstrated in a short estimation by assuming a Q-value measurement of two isobars: In this case, the frequency ratio is almost 1 and hence $r - 1 \to 0$, which lowers the influence of the error of the mass of the daughter nuclide by several orders of magnitude. In the following, we still take this uncertainty into account for the sake of completeness for measurements without isobars and obtain:

$$u(Q) = \sqrt{[m_d \cdot u(r)]^2 + [(r-1) \cdot u(m_d)]^2} \,. \tag{5.28}$$

In total, the lower limit for the accuracy of the Q-values $u(Q)$ is much lower than the accuracy of the mass measurement $u(m)$ since the uncertainty of the reference ion $u(m_d)$

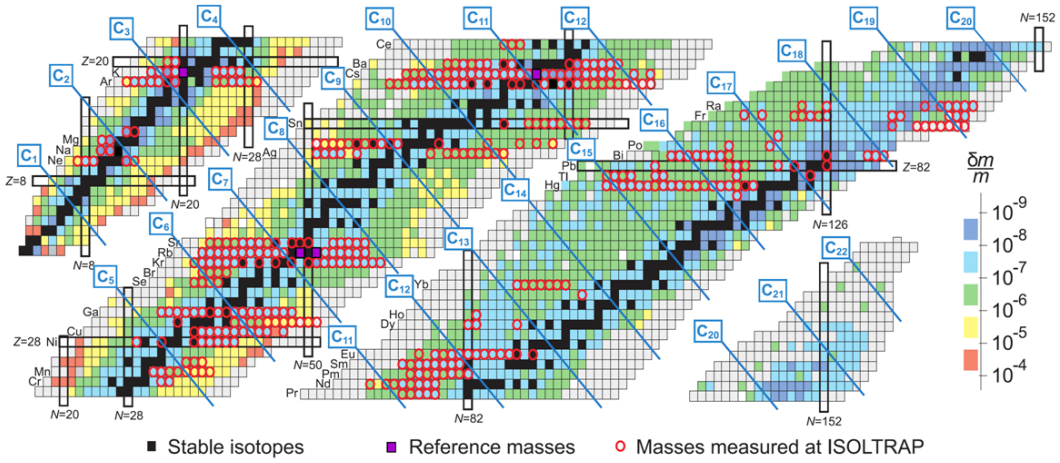

Figure 5.2: Table of nuclei were the relative uncertainties of the masses are indicated by a color code. Furthermore, the nuclei measured at ISOLTRAP (red), the alkali reference ions (purple) and the "mass grid", which shows the isobaric lines of the carbon clusters $^{12}C_i$ (blue lines) are shown. [Bla05]

or the daughter nuclide $u(m_{ref})$, the residual uncertainty $\frac{u_{res}}{r}$, and the mass-dependent systematic effect $\frac{u_m}{r}$ can be neglected. In addition, the uncertainty can be lowered by using the polynomial method instead of the interpolation method in order to lower the uncertainty of the frequency ratio Δr. For this reason, the high-precision Q-value measurements presented later are evaluated by the polynomial method.

5.1.4 Carbon Clusters as Reference Masses

Carbon clusters are the ideal choice for reference masses in accurate mass measurements with Penning traps [Bla02, Bla03]. Some of the uncertainties in mass determination mentioned above can be either neglected or reduced by the use of carbon clusters. First of all, the uncertainty of the frequency ratio depends on the mass-dependent ratio shift (see eq.(5.24)). Here, the shift is proportional to the difference in mass between the reference ion and the ion of interest $m - m_{ref}$. In case of carbon clusters $^{12}\mathrm{C}_i$, which are multiples of $^{12}\mathrm{C}$ one can always find a reference ion, which is maximally 6 mass units away from the ion of interest and hence, the systematic mass-dependent ratio shift is minimized. Fig. 5.2 shows the nuclear chart and the overlayed "mass grid" of the carbon clusters, which shows the isobaric lines of the carbon clusters $^{12}C_i$. Furthermore, the uncertainty of the mass of a carbon cluster is by definition almost zero since the atomic mass unit is defined as 1/12 of the mass of the $^{12}\mathrm{C}$ isotope and the atomic binding energy can be neglected or even corrected for.

5.2 Masses of ^{110}Pd and ^{110}Cd

5.2.1 Experimental Procedure

The masses of ^{110}Pd and ^{110}Cd were measured using the $^{12}C_{11}$ clusters as reference. $^{12}C_{11}$ was chosen for the sake of simplicity because the clusters closer in mass to $A = 110$, $^{12}C_8$, $^{12}C_9$, and $^{12}C_{10}$, could not be produced with sufficient numbers at that time. All ions were produced by laser ablation with the ISOLTRAP laser ion source, as described in detail in chapter 4. In order to change the element, the sample holder was turned manually. Here, the starting positions and hence, also the starting conditions of the ions differed slightly from element to element due to small, unavoidable differences of the alignment and the pellet preparation of the different elements. Thus, the optimal settings of the ion optics for the ion transfer from the laser ion source to the preparation trap had to be determined for each element and were adjusted after every change of the element. Furthermore, the optimal laser power densities for a stable and sufficient ion production for those measurements were determined to $\rho_{\mathrm{Pd}} = 11.0(5) \cdot 10^7\,\mathrm{W/cm^2}$ ($E_{pulse} = 18.8(9)\,\mathrm{mJ}$), $\rho_{\mathrm{Cd}} = 6.0(3) \cdot 10^7\,\mathrm{W/cm^2}$ ($E_{pulse} = 10.8(6)\,\mathrm{mJ}$), and $\rho_{^{12}\mathrm{C}_{11}} = 4.7(2) \cdot 10^7\,\mathrm{W/cm^2}$ ($E_{pulse} = 8.51(5)\,\mathrm{mJ}$), where errors of about 5% were assumed. All measurements devoted to mass determination were based on a $(50-600-50)$ ms Ramsey excitation scheme with an average time of about 15 min per resonance. For both mass measurements of ^{110}Pd and ^{110}Cd, four $(50-600-50)$ ms resonances of the ion of interest and five reference measurements with $^{12}C_{11}$ clusters were taken.

5.2.2 Experimental Results: Cyclotron Frequency-Ratio and Mass Determination

The cyclotron frequencies ν and their standard deviations $s(\nu)$ were determined by a fit of the expected line shape to the data [Kre07], as described in chapter 3.2.3. Here, only events with fewer than 10 detected ions were taken into account in order to avoid frequency shifts due to contamination and field disturbances (see section 5.1.2). Then, the frequency ratios r of the ions of interest and the reference ions, as well as their standard uncertainties u_{int} were obtained by the interpolation method (see section 5.1.1). According to eq. (5.24), also the systematic mass shift u_m and the residual uncertainty had to be taken into account because the masses of the $^{12}C_{11}$ clusters and the ^{110}Pd and ^{110}Cd ions differ by 22 mass units. The masses themselves were calculated using eq. (5.26). Here, the uncertainty of the $^{12}C_{11}$ reference mass can be neglected because it is almost zero, as described in section 5.1.4. In the following, instead of the mass of atom ${}^A_Z\mathrm{X}$ with atomic number Z and atomic mass number A, we will use the the mass excess ME, which is defined as the difference of the actual mass of the atom $m({}^A_Z\mathrm{X})$ and its atomic mass number A:

$$ME({}^A_Z\mathrm{X}) = A \cdot u - m({}^A_Z\mathrm{X})\,. \tag{5.29}$$

Fig. 5.3 a) and fig. 5.3 b) show the individual frequency ratios r^i for ^{110}Pd and ^{110}Cd, respectively. The final experimental results of the mass measurements of ^{110}Pd and ^{110}Cd

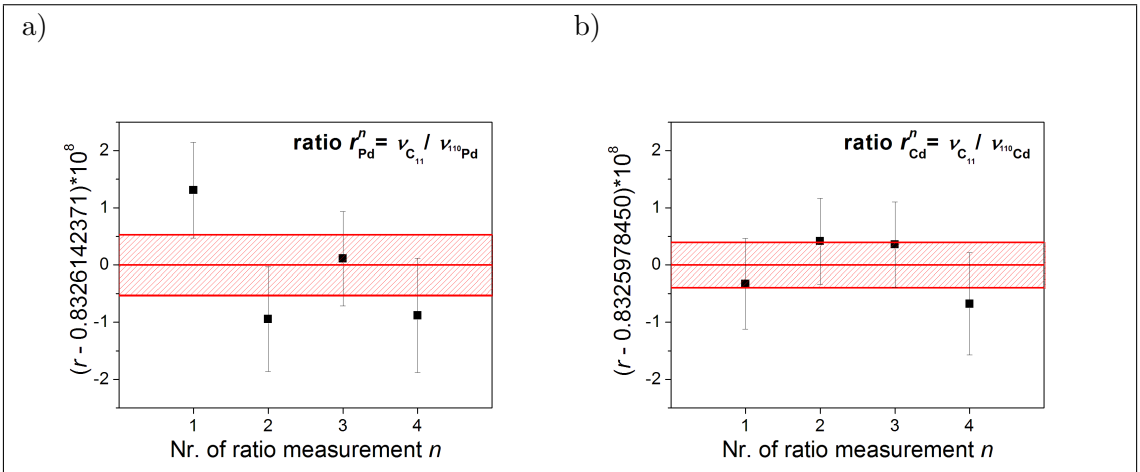

Figure 5.3: a) The distribution of the individual cyclotron frequency-ratio measurements of ^{110}Pd and $^{12}C_{11}$. The dashed area represents the standard deviation of the mean value. b) The same distribution for measurements of ^{110}Cd and $^{12}C_{11}$.

are summarized in tab. 5.1. Here, the first column shows the mean cyclotron frequency ratios of ^{110}Pd and ^{110}Cd to the $^{12}C_{11}$ reference ion. The values in brackets are the three components of the ratio uncertainty (see eq. (5.24)): the statistical uncertainty for the interpolation method u_{int}, the systematic mass effect u_m, and the residual systematic uncertainty u_{res}. The second column lists the resulting mass excesses, while the third column lists the literature values from the last atomic-mass evaluation AME2003 [Aud03].

Table 5.1: The mean cyclotron frequency ratios $\overline{r}$ of ^{110}Pd and ^{110}Cd to the $^{12}C_{11}$ carbon cluster and the resulting mass excess values (ME). The statistical uncertainty (u_{int}), the mass-dependent systematic effect (u_m) and the residual systematic uncertainty (u_{res}) are specified for the cyclotron ratios. The last column lists the literature values of the last atomic-mass evaluation AME2003 [Aud03].

Nuclide	$\overline{r}$ (u_{int}) (u_m) (u_{res})	ME_{exp} / keV	ME_{lit} / keV [Aud03]
^{110}**Pd**	0.8326142342(53)(35)(82)	**-88332.89(78)**	-88353.25(6.73)
^{110}**Cd**	0.8325978421(39)(35)(82)	**-90348.41(65)**	-90352.37(2.23)

5.2.3 Discussion

Fig. 5.4 shows the experimental results of the mass measurements of ^{110}Pd and ^{110}Cd together with the literature values from the latest atomic-mass evaluation AME2003. The values given in AME2003 are a weighted average of measurements. In fig. 5.4 a)

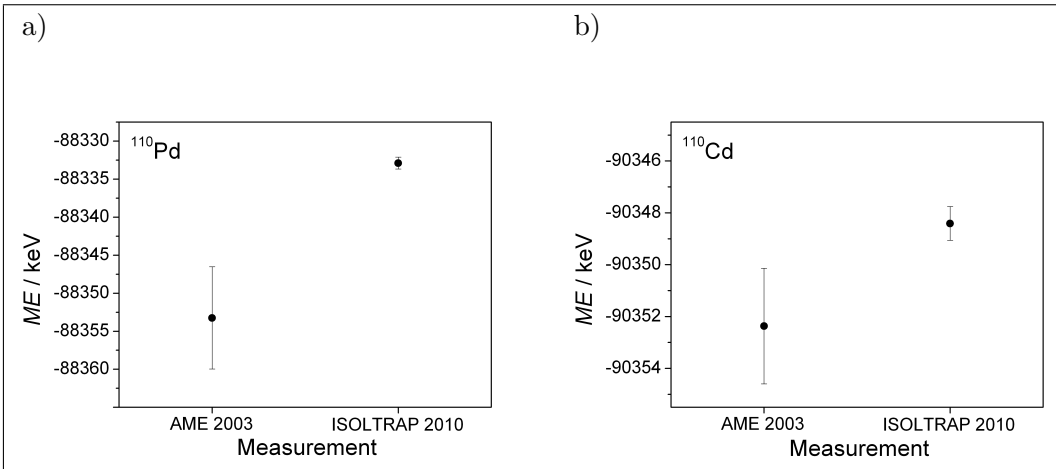

Figure 5.4: a) The experimentally obtained mass excess of ^{110}Pd and its literature value from AME2003 [Aud03]. b) The same for the mass excess of ^{110}Cd.

the experimental value of the 2010 ISOLTRAP measurement and the literature value of the AME2003 of the mass excess of ^{110}Pd are shown. The ISOLTRAP value differs from the literature value by 20.36 keV (ca. 3σ). However, we obtained similar results during the Q-value measurements of the ^{110}Cd-^{110}Pd transition, presented in the next section, if the ^{110}Cd isotope is taken as the reference ion to determine the mass of ^{110}Pd. Here, the resulting mass excess values were $ME = -88334.75(2.71)$ keV in case of the $(30 - 840 - 30)$ ms Ramsey excitation and $ME = -88335.77(2.71)$ keV in case of the $(50 - 600 - 50)$ ms Ramsey excitation, which agree within the errors with the 2010 ISOLTRAP mass measurement on ^{110}Pd with carbon clusters as reference, as listed in tab. 5.1. Because no obvious problems are visible in previous measurements, the experiment should be repeated at comparable Penning trap mass spectrometers such as the double Penning trap system TRIGA-TRAP [Ket08], which has a similar laser ion source compared to the ISOLTRAP source. In contrast to the mass excess of ^{110}Pd, the mass excess value of ^{110}Cd agrees within 1.5σ with the literature value of the atomic-mass evaluation AME2003. Here, the obtained uncertainty of the mass excess is more than three times smaller than the value given in AME2003. Finally, it should be noted that the studies on ^{110}Pd and ^{110}Cd presented here, are the first atomic masses measured at ISOLTRAP where the carbon cluster species were used as reference.

5.3 The Q-Value of the ^{110}Pd and ^{110}Cd Mass Doublet

5.3.1 Experimental Procedure

In order to measure the Q-value of the ^{110}Pd and ^{110}Cd mass doublet, the ions were produced similarly to the ion production for the mass measurements of ^{110}Pd and ^{110}Cd by laser ablation with the ISOLTRAP laser ion source as described in section 4 and 5.2.1.

The cyclotron frequencies of the $^{110}Cd^{+}$ and $^{110}Pd^{+}$ ions were measured alternately over a longer period in order to obtain a sufficient number of data points to be able to employ the polynomial method, as described in section 5.1.1. In total, two different data sets were recorded one after another using the Ramsey method to test the reliability of the system under several conditions. First a $(30-840-30)$ ms Ramsey excitation scheme and later a $(50-600-50)$ ms excitation scheme was applied. Several conventional 900 ms resonances were taken during the measurements, to determine the center frequency of the Ramsey ToF spectrum. 17 cadmium measurements and 16 palladium measurements were performed in both cases. The overall measuring time was about 19 hours in the case of the $(30-840-30)$ ms Ramsey excitation scheme and about 15 hours in the case of the $(50-600-50)$ ms Ramsey excitation scheme.

5.3.2 Experimental Results: Cyclotron frequency-ratio and Q-Value Determination

The cyclotron frequencies and their standard deviations in individual ToF resonances were determined similarly as in the mass measurements of ^{110}Pd and ^{110}Cd (see section 5.2.2) by a fit to the expected line shape [Kre07]. Next, the cyclotron frequency ratio and its uncertainties in the two data sets were determined by the polynomial method, as described in section 5.1.1. Eq. (5.11) was fited to the ^{110}Cd data, while eq. (5.12) was fitted to the ^{110}Pd data at the same time. Fig. 5.5 shows the drift of the cyclotron frequencies of ^{110}Pd and ^{110}Cd due to the fluctuations of the magnetic field in time, as described in 5.1.2, and the corresponding polynomial fits. As described in section 5.1.3, the statistical uncertainty of the cyclotron frequency ratio obtained by the polynomial method represents the total uncertainty of the ratio since the behavior of the magnetic field is already taken into account by the polynomials (see eq. (5.11) and eq. (5.12). Next, the Q-values of both data sets were calculated by eq. (5.2), while their uncertainties were calculated by eq. (5.28). The resulting values are listed in tab. 5.2. The final Q-value is the weighted average (including the scattering of the data) of both measurements, which is given in the third row. In addition, the literature value of the Q-value, which is calculated by eq. (2.27) using the mass excess values of ^{110}Pd and ^{110}Cd of the last atomic-mass evaluation AME2003 [Aud03], is shown in the last row of the table. Its uncertainty is calculated by the Gaussian error propagation.

5.3.3 Discussion

Both experimentally obtained values from the two Ramsey data sets agree within 1.3σ. The final value of the ISOLTRAP Q-value measurement of the ^{110}Pd and ^{110}Cd mass doublet is the weighted average value of both data sets $Q = 2017.78(34)$ keV. The weighted average differs by 18.66 keV from the literature value, which can be explained by the discrepancy of 20.36 keV between the experimental value and the literature value of the mass of ^{110}Pd as described in section 5.2.3.
In total, the uncertainty of the Q-value of the ^{110}Pd-^{110}Cd transition could be reduced by a factor of close to 30 to an uncertainty of 340 eV, with respect to the literature

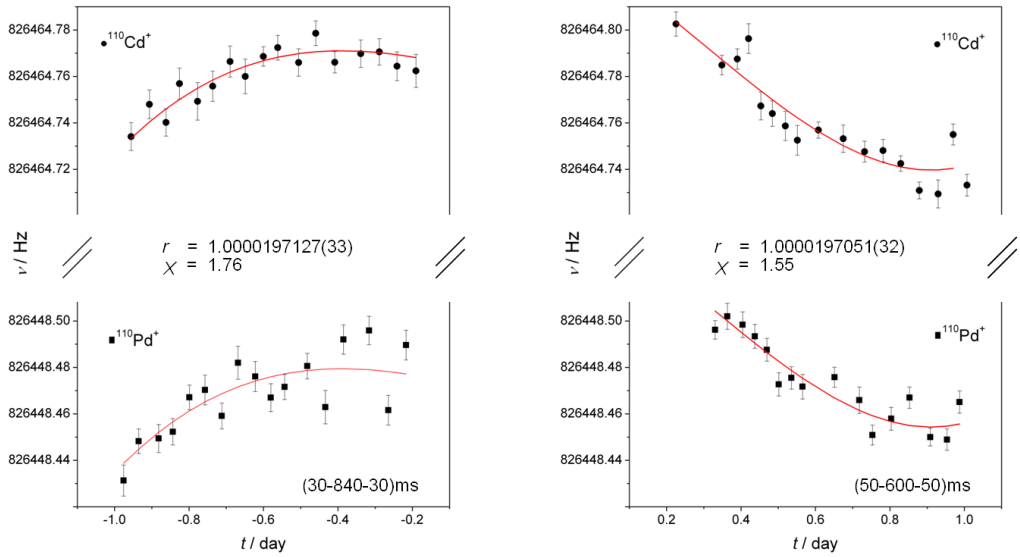

Figure 5.5: The two data sets and their behavior in time due to the magnetic field fluctuations. Here, the time origin is set between the two data sets to reduce the influence of the time variable to the fit parameters. The cyclotron frequency ratio r is obtained as a fit parameter. a) Shows the behavior of the measurements with the $(30 - 840 - 30)$ ms Ramsey excitation. The solid lines are the fitted polynomials (eq. 5.11 and eq. 5.12) to the data. b) Shows the same for the data with $(50 - 600 - 50)$ ms Ramsey excitation.

Table 5.2: The results of the evaluation of the Q-value measurements of the ^{110}Pd and ^{110}Cd mass doublet. The second column lists the cyclotron frequency ratios obtained by the polynomial method, while the third column lists the Q-values. In addition to the two data sets, the weighted average of both data sets is given in the third row and the literature value, calculated by the mass excess values of AME2003 [Aud03], is given in the fourth row.

Data	ratio r	^{110}Pd/^{110}Cd Q-value / keV
$(30 - 840 - 30)$ ms Ramsey	1.0000197127(33)	2018.07(34)
$(50 - 600 - 50)$ ms Ramsey	1.0000197051(32)	2017.29(32)
Weighted average	-	**2017.78(34)**
AME2003	-	1999.12(9.13)

value of AME2003. Thus, it provides a key parameter for future experiments on the search for the decay signal of the neutrinoless double beta decay of the ^{110}Pd-^{110}Cd transition. Furthermore, it will allow more precise calculations of the phase space G and the matrix elements of both decays, the neutrino accompanied double beta decay and the neutrinoless double beta decay of this mass doublet.

6 Summary and Outlook

Within this work, I have presented the mass and Q-value measurements of the mass doublet and double beta decay candidate ^{110}Pd/^{110}Cd. These studies were the first of this type at the double Penning trap mass spectrometer ISOLTRAP at the on-line mass separator ISOLDE/CERN. For this purpose, the ISOLTRAP laser ablation ion source was modified and characterized in order to produce the $^{110}Pd^{+}$ and $^{110}Cd^{+}$ ions. In addition, the production of carbon clusters could be demonstrated and used for the first time as references for mass measurements at ISOLTRAP.
A high-precision Q-value is of outmost important to identify the signal of the neutrinoless double beta decay in future experiments. Up to now, no unambiguous signal of this hypothetic nuclear decay was found for any candidate yet. Neutrinoless double beta decay requires massive Majorana neutrinos and is not allowed by the Standard Model, because it violates the total lepton number conservation by two units. However, there are strong reasons to assume that this nuclear decay exists. Its discovery would allow an absolute measurement of the neutrino mass and would provide a deep insight into the mechanisms of physics beyond the Standard Model.
An ideal tool for high-precision mass and Q-value measurements is a Penning trap mass spectrometer. Here, the ion is trapped in a magnetic field and a perpendicular electrical quadrupole field. The mass or the Q-value can be obtained from the cyclotron frequency ω_c, which depends on the mass, the charge, and the magnetic field in the trap. A typical measurement cycle consists of a measurement of the ion of interest and a reference ion with a well-known mass to calibrate the magnetic field. The cyclotron frequency itself is measured by the destructive TOF-ICR detection. Besides the conventional ToF detection, the Ramsey excitations can be used in this work for determining ω_c, which has the advantage of an increased resolving power.
The mass and Q-value measurements presented in this thesis took place at the double Penning trap mass spectrometer ISOLTRAP. The main parts of the setup are the radiofrequency ion beam cooler and buncher, the preparation Penning trap, and the precision Penning trap. In addition to the ions coming from ISOLDE, a surface ion source and a laser ablation ion source are installed to deliver ions for reference measurements or for off-line experiments.
An important part of this thesis besides the mass and Q-value measurements of the ^{110}Pd/^{110}Cd mass doublet was the modification and characterization of the ISOLTRAP laser ion source in order to produce the studied ions. Laser ionization at ISOLTRAP is based on the laser ablation principle. Here, a laser pulse with a high energy is shot on a solid target and generates a plasma plume of the material, where the ions are created. Since the ion production is very sensitive to the irradiated laser energy, the old laser was replaced by a new laser with a better pulse-to-pulse stability. Furthermore, the

laser optics was extended and rearranged so that the laser pulses are not shot on the sample at an angle of 45° any more, but perpendicular to it in order to improve the handling of the laser source and the starting conditions of the ablated ions. Next, the laser focus diameter at the pellet position was determined by the knife-edge method. A slightly elliptic beam profile was obtained with a ratio of $w_{ver}/w_{hor} = 1/1.8$ between the vertical and horizontal direction. The maximum laser power density with the presently installed laser and laser optics was determined to be $1.00 \cdot 10^9\,\mathrm{W/cm^2}$. In order to produce the ions in the ion optics axis and hence, improve the starting conditions, the sample holder was moved out off the ion optics axis. Therefore, several elements such as the holder of the aluminum disc and some flanges were shifted out of axis by 5 mm. Several new ion optics elements were designed, simulated by SIMION© and tested. With the new setup of the laser ion source, the production and ionization of the stable palladium and cadmium isotopes as well as the $^{12}C_n^+$ carbon clusters from $n = 3$ to $n = 24$ could be demonstrated. Optimal laser power densities for a stable production of a sufficient number of ions were determined to $9.4(5) \cdot 10^7\,\mathrm{W/cm^2}$ for palladium ions, $6.2(3) \cdot 10^7\,\mathrm{W/cm^2}$ for cadmium ions, and $\rho = 4.6(2) \cdot 10^7\,\mathrm{W/cm^2}$ for carbon clusters. Furthermore, an illustration of the ion production, selection, and excitation process at ISOLTRAP was given on the example of the palladium isotope $^{110}Pd^+$. Now, the laser ablation ion source is working reliably and is in permanent use.
One main uncertainty in cyclotron frequency measurements are the fluctuations of the magnetic field in time, which has to be considered by the data evaluation method. Within this thesis, two methods to evaluate the data were applied: the conventionally used interpolation method and the polynomial method, which was used for the first time at ISOLTRAP. One measurement cycle of the interpolation method consists of two measurements of the cyclotron frequency of the reference ion and one measurement of the cyclotron frequency of the ion of interest. The reference ion is measured just before and after the ion of interest to reduce the effect of the drift of the magnetic field. In the evaluation process, the frequency of the reference ion is interpolated to the time, when the ion of interest was measured in order to compensate the fluctuations of the magnetic field. To apply the polynomial method, the cyclotron frequencies of the reference ion and the ion of interest have to be measured several times alternately. To evaluate the data, two polynomials are fitted to the data set simultaneously, where the ratio of both cyclotron frequencies can be obtained as a fit parameter, from which the Q-value and the mass can be derived. The advantage of the polynomial method is that several uncertainties can be neglected and the final uncertainty is lower than with the interpolation method.

The masses of ^{110}Pd and ^{110}Cd were determined by the interpolation method using carbon clusters as reference. The final mass excess value is $-88332.89(78)\,\mathrm{keV}$ for ^{110}Pd and $-90348.41(65)\,\mathrm{keV}$ for ^{110}Cd. While the mass excess value of ^{110}Cd agrees with the literature value within 1.5σ and differs only by around 4 keV, the mass excess value of ^{110}Pd differs by more than 20 keV and 3σ to the literature value. Further studies should investigate on the discrepancy between both values.
To determine the Q-value, two data sets with two different Ramsey excitation times

were taken with 33 ToF resonances of $^{110}Pd^{+}$ and $^{110}Cd^{+}$ each. The cyclotron ratios were determined for both data sets by the polynomial method and the final value is the weighted mean value of the Q-values of both measurements. Within this thesis, the final Q-value of the $^{110}Pd/^{110}Cd$ mass doublet could be determined to 2017.78(34) keV. Its uncertainty is 26 times smaller than the uncertainty of the present literature value obtained from atomic-mass evaluation AME2003.
In the near future, the mass measurements on ^{110}Pd will be repeated at an experimental setup similar to ISOLTRAP, such as the TRIGA-TRAP mass spectrometer, in order to investigate on the discrepancy between the mass excess value obtained from the ISOLTRAP measurements and the literature value.
Furthermore, the laser ion source will be further prepared and optimized for the daily use in on-line mass measurements at ISOLTRAP as a carbon cluster reference ion source. With carbon clusters as references, one will be able to take advantage of the negligible mass uncertainty of the carbon clusters. Also, the carbon clusters spread over the whole nuclear table with a maximum distance in mass of 6 mass units to every isotope, which reduces the uncertainty due to the mass-dependent systematic effect and the systematic residual uncertainty.
The setup, presented in this work, allows further measurements on palladium and cadmium isotopes. It was shown that all stable palladium and cadmium isotopes as well as many carbon cluster sizes are producible with the laser ablation ion source and the current sample configuration. In principle, high-precision mass measurements of all other stable palladium isotopes ^{102}Pd, ^{104}Pd, ^{105}Pd, ^{106}Pd, and ^{108}Pd as well as all other stable cadmium isotopes ^{106}Cd, ^{108}Cd, ^{111}Cd, ^{112}Cd, and ^{114}Cd are possible using carbon clusters as reference masses. At the moment, the uncertainties of the mass excesses are in the range from 2.7 keV in case of $^{110,112,114}Cd$ to up to 6 keV in case of ^{106}Cd [Aud03].

In addition, there are two other double beta decay palladium and cadmium mass doublets, which can be produced by the current ISOLTRAP laser ablation ion source and its pellet configuration. One is the possible double beta isotope ^{108}Cd. However, its Q-value is lower than 1 keV, which leads to a very long half-life, which makes the observation of its neutrino less double decay very challenging.
A very interesting isotope is ^{106}Cd, which is a possible candidate for double positron decay. The $^{106}Cd/^{106}Pd$ mass doublet has a high Q-value of more than 2780 keV [Zub04]. Even though the available phase space is reduced by 2048 keV due to four electron masses (see chapter 2.2.1), there is still the possibility that the half-life is shortened by several orders of magnitude due to a resonance of the ground state of the mother nuclide ^{106}Cd and an excited state of the daughter nuclide ^{106}Pd. The goal of the upcoming studies on this transition at ISOLTRAP is an uncertainty of the Q-value down to 200 eV.

Bibliography

[Ahm02] Ahmad, Q. R. et al.: Direct evidence for neutrino flavor transformation from neutral-current interactions in the Sudbury Neutrino Observatory. In: *Phys. Rev. Lett.* 89 (2002), p. 011301

[Ahm04] Ahmed, S. et al.: Measurement of the total active ^{8}B solar neutrino flux at the Sudbury Neutrino Observatory with enhanced neutral current sensitivity. In: *Phys. Rev. Lett.* 92 (2004), p. 181301

[And62] Anderson, P. W.: Theory of flux creep in hard superconductors. In: *Phys. Rev. Lett.* 9 (1962), p. 309–311

[And64] Anderson, P. W. ; Kim, Y. B.: Hard superconductivity: Theory of the motion of Abrikosov flux lines. In: *Rev. Mod. Phys.* 36 (1964), p. 39–43

[Ans95] Anselmann, P. et al.: GALLEX solar neutrino observations: Complete results for GALLEX II. In: *Phys. Lett. B* 357 (1995), p. 237–247

[Aud03] Audi, G. ; Wapstra, A. H. ; Thibault, C.: The 2003 atomic mass evaluation. In: *Nucl. Phys. A* 729 (2003), p. 129 – 676

[Bec93] Beck, D.: *Aufbau einer zylindrischen Penningfalle zum Einfang und Kühlen von Ionen*, Johannes Gutenberg-Universität Mainz, Diploma Thesis, 1993

[Bet36] Bethe, H. A. ; Bacher, R. F.: Stationary states of nuclei. In: *Rev. Mod. Phys.* 8 (1936), p. 82–229

[Böh09] Böhm, C.: *Setup of a carbon-cluster laser ion source and the application of the invariance theorem at ISOLTRAP*, Johannes Gutenberg-Universität Mainz, Diploma Thesis, 2009

[Bla02] Blaum, K. et al.: Carbon clusters for absolute mass measurements at ISOLTRAP. In: *Eur. Phys. J. A* 15 (2002), p. 245–248

[Bla03] Blaum, K. et al.: Cluster calibration in mass spectrometry: laser desorption/ionization studies of atomic clusters and an application in precision mass spectrometry. In: *Anal. Bioanal. Chem* 36 (2003), p. 921–930

[Bla05] Blaum, K. et al.: ISOLTRAP mass measurements of exotic nuclides at $\delta m/m = 10^{-8}$. In: *Nucl. Phys. A* 752 (2005), p. 317 – 320

[Bla06] Blaum, K.: High-accuracy mass spectrometry with stored ions. In: *Phys. Rep.* 425 (2006), p. 1–78

[Bol92] Bollen, G. et al.: Resolution of nuclear ground and isomeric states by a Penning trap mass spectrometer. In: *Phys. Rev. C* 46 (1992), p. 2140–2143

[Bol96] Bollen, G. et al.: ISOLTRAP: A tandem Penning trap system for accurate on-line mass determination of short-lived isotopes. In: *Nucl. Instrum. Meth. A* 368 (1996), p. 675 – 697

[Bol01] Bollen, G.: Mass measurements of short-lived nuclides with ion traps. In: *Nucl. Phys. A* 693 (2001), p. 3 – 18

[Bro82] Brown, L. S. ; Gabrielse, G.: Precision spectroscopy of a charged particle in an imperfect Penning trap. In: *Phys. Rev. A* 25 (1982), p. 2423–2425

[Bro86] Brown, L. S. ; Gabrielse, G.: Geonium theory: Physics of a single electron or ion in a Penning trap. In: *Rev. Mod. Phys.* 58 (1986), p. 233–311

[Cha93] Chapple, P. B.: Beam waist and m2 measurement using a finite slit. In: *Opt. Eng.* 33 (1993), p. 2461–2466

[Col00] Collaboration, GNO: GNO solar neutrino observations: Results for GNO I. In: *Phys. Lett. B* 490 (2000), p. 16–26

[Col02] Collaboration, The Super-Kamiokande: Determination of solar neutrino oscillation parameters using 1496 days of Super-Kamiokande-I Data. In: *Phys. Lett. B* 539 (2002), p. 179–187

[Dan62] Danby, G. et al.: Observation of high-energy neutrino reactions and the existence of two kinds of neutrinos. In: *Phys. Rev. Lett.* 9 (1962), Nr. 1, p. 36–44

[Dav94] Davis, R. et al.: A review of the Homestake solar neutrino experiment. In: *Prog. Part. Nucl. Phys.* 32 (1994), p. 13–32

[Dav03] Davis, R.: A half-century with solar neutrinos (nobel lecture). In: *ChemPhysChem* 4 (2003), p. 662–671

[Deh90] Dehmelt, H.: Experiments with an isolated subatomic particle at rest. In: *Rev. Mod. Phys.* 62 (1990), p. 243

[Doi85] Doi, M. ; Kotani, T. ; Takasugi, E.: Double beta decay and Majorana neutrino. In: *PTP* 83 (1985), p. 1–175

[Dou01] Douysset, G. et al.: Determination of the ^{76}Ge double beta decay Q-value. In: *Phys. Rev. Lett.* 86 (2001), p. 4259–4262

[Ell87] Elliott, S. R. ; Hahn, A. A. ; Moe, M. K.: Limit on neutrinoless double-beta decay with majoron emission in ^{82}Se. In: *Phys. Rev. Lett.* 59 (1987), p. 1649–1651

[Fur39] Furry, W. H. et al.: On transition probabilities in double beta-disintegration. In: *Phys. Rev.* 56 (1939), p. 1184–1193

[Geo07] George, S. et al.: Ramsey method of separated oscillatory fields for high-precision Penning trap mass spectrometry. In: *Phys. Rev. Lett.* 98 (2007), p. 162501

[Gla80] Glashow, S. L.: Towards a unified theory: Threads in a tapestry. In: *Rev. Mod. Phys.* 52 (1980), p. 539–543

[GM35] Goeppert-Mayer, M. et al.: Double beta-disintegration. In: *Phys. Rev.* 48 (1935), p. 512–516

[Grä80] Gräff, G. ; Kalinowsky, H. ; Traut, J.: A direct determination of the proton electron mass ratio. In: *Z. f. Phys. A* 297 (1980), p. 35–39

[Gue97] Guenther, M. et al.: Heidelberg-Moscow double beta experiment with ^{76}Ge: Full setup with five detectors. In: *Phys. Rev. D* 55 (1997), p. 54–67

[Her01] Herfurth, M. et al.: A linear radiofrequency ion trap for accumulation, bunching, and emittance improvement of radioactive ion beams. In: *Nucl. Instrum. Meth. A* 469 (2001), p. 254 – 275

[Hir90] Hirata, K. et al.: Constraints on neutrino-oscillation parameters from the Kamiokande-II solar neutrino data. In: *Phys. Rev. Lett.* 65 (1990), p. 1301–1304

[Hir94] Hirsch, M. et al.: Nuclear structure calculation of $\beta^+\beta^+$, β^+/EC and EC/EC decay matrix elements. In: *Z. f. Phys. A* 347 (1994), p. 151–160

[KAT05] *KATRIN design report 2004*. 2005

[Kel03] Kellerbauer, A. et al.: From direct to absolute mass measurements: A study of the accuracy of ISOLTRAP. In: *Eur. Phys. J. D* 22 (2003), p. 53–64

[Ket99] Ketterson, J. B. ; Song, S. N.: *Superconductivity*. Cambridge University Press, Cambridge 1999

[Ket08] Ketelaer, J. et al.: TRIGA-SPEC: A setup for mass spectrometry and laser spectroscopy at the research reactor TRIGA Mainz. In: *Nucl. Instrum. Meth. A* 594 (2008), p. 162 – 177

[KK04] Klapdor-Kleingrothaus, H. V. et al.: Search for neutrinoless double beta decay with enriched ^{76}Ge in Gran Sasso 1990-2003. In: *Phys. Lett. B* 586 (2004), p. 198 – 212

[Kön95] König, M. et al.: Quadrupole excitation of stored ion motion at the true cyclotron frequency. In: *Int. J. of Mass Spectr.* 142 (1995), p. 95 – 116

[Kod01] Kodama, K. et al.: Observation of tau neutrino interactions. In: *Phys. Lett. B* 504 (2001), p. 218 – 224

[Kow10] Kowalska, M.: ISOLTRAP results 2006–2009. In: *Hyperfine Interact.* 196 (2010), p. 199–203

[Kre92] Kretzschmar, M.: Single particle motion in a Penning trap: Description in the classical canonical formalism. In: *Physica Scripta* 46 (1992), p. 6

[Kre07] Kretzschmar, M.: The Ramsey method in high-precision mass spectrometry with Penning traps: Theoretical foundations. In: *International Journal of Mass Spectrometry* 264 (2007), p. 122 – 145

[Kös03] Köster, U. ; Fedoseyev, V. N. ; Mishin, V. I.: Resonant laser ionization of radioactive atoms. In: *Spectrochim. Acta B* 58 (2003), p. 1047 – 1068

[Kug00] Kugler, E.: The ISOLDE facility. In: *Hyperfine Interact.* 129 (2000), p. 23–42

[Mau04] Maul, J.: *Ortsaufgelöster Nachweis von Elementspuren mittels Laserablation und Resonanzionisations-Massenspektrometrie und Untersuchungen zur Laserablations-Dynamik*, Johannes Gutenberg-Universität Mainz, Diss., 2004

[Muk08] Mukherjee, M. et al.: ISOLTRAP: An on-line Penning trap for mass spectrometry on short-lived nuclides. In: *Eur. Phys. J. A* 35 (2008), p. 1–29

[Ott08] Otten, E. W. ; Weinheimer, C: Neutrino mass limit from tritium β-decay. In: *Rep. Prog. Phys.* 71 (2008), p. 086201–086237

[Pau77] Pauli, W.: *Fünf Arbeiten zum Ausschließungsprinzip und zum Neutrino.* Wissenschaftliche Buchgesellschaft Darmstadt, Darmstadt 1977

[Pie49] Pierce, J.R.: *Theory and design of electron beams.* D. van Nostrand Co., New York 1949

[Rah08] Rahaman, S. et al.: Q-values of the ^{76}Ge and ^{100}Mo double-beta decays. In: *Phys. Let. B* 662 (2008), p. 111 – 116

[Rah09] Rahaman, S. et al.: Accurate Q-value for the ^{112}Sn $\beta\beta$-decay and its implication for the search of the neutrino mass. In: *Phys. Rev. Lett.* 103 (2009), p. 042501

[Red07] Redshaw, M. et al.: Mass and double-beta-decay Q-value of ^{136}Xe. In: *Phys. Rev. Lett.* 98 (2007), p. 053003

[Red09] Redshaw, M. et al.: Masses of ^{130}Te and ^{130}Xe and $\beta\beta$-decay Q-value of ^{130}Te. In: *Phys. Rev. Lett.* 102 (2009), p. 212502

[Rei56] Reines, F. ; Cowan, C. L.: The neutrino. In: *Nature* 178 (1956), p. 446–449

[Rus04] Russo, R. E. et al.: Laser assisted plasma spectrochemistry: Laser ablation. In: *J. Anal. Atom Spectrom* 19 (2004), p. 1084–1089

[Sal80] Salam, Abdus: Gauge unification of fundamental forces. In: *Rev. Mod. Phys.* 52 (1980), p. 525–538

[Sav91] Savard, G. et al.: A new cooling technique for heavy ions in a Penning trap. In: *Phys. Lett. A* 158 (1991), p. 247 – 252

[Sco35] Scott, F. A.: Energy spectrum of the beta-rays of radium E. In: *Phys. Rev.* 48 (1935), p. 391–395

[Seg77] Segrè: *Nuclei and particles. An introduction to nuclear and subnuclear physics.* Benjamin, New York 1977

[Tor03] Torrisi, L. et al.: Comparison of nanosecond laser ablation at 1064 and 308 nm wavelength. In: *Appl. Surf. Sci.* 210 (2003), p. 262 – 273

[VD92] Van Dyck, R. S. J. ; Farnhama, D. L. ; Schwinberga, P. B.: A compensated Penning trap mass spectrometer and the ^{3}H-^{3}He mass difference. In: *J. Mod. Opt.* 39 (1992), p. 243 – 255

[Wei80] Weinberg, Steven: Conceptual foundations of the unified theory of weak and electromagnetic interactions. In: *Rev. Mod. Phys.* 52 (1980), p. 515–523

[Wei05] Weizsäcker, C. F.: Zur Theorie der Kernmassen. In: *Z. f. Phys.* 96 (2005), p. 431–458

[Win52] Winter, R. G.: A search for double beta-decay in palladium. In: *Phys. Rev.* 85 (1952), p. 687

[Wri92] Wright, D. et al.: Laser beam width, divergence and beam propagation factor – an international standardization. In: *Opt. Quant. El.* 24 (1992), p. 993–1000

[Yaz06] Yazidjian, C. et al.: A new Channeltron-detector setup for precision mass measurements at ISOLTRAP. In: *Hyperfine Interact.* 173 (2006), p. 181–193

[Zub98] Zuber, K.: On the physics of massive neutrinos. In: *Phys. Rep.* 305 (1998), p. 295–364

[Zub04] Zuber, K.: Double beta decay. In: *Contemp Phys.* 45 (2004), p. 295–364

Danksagung

An dieser Stelle möchte ich mich noch einmal bei den folgenden Personen und Einrichtungen persönlich bedanken:
Klaus Blaum dafür, dass er mir diese spannende Diplomarbeit bei ISOLTRAP und die Erfahrung am CERN ermöglicht hat. Sowie für die tolle Unterstützung mit Rat, Tat und Geduld von Anfang bis Ende.
Magdalena Kowalska und *Susanne Kreim* für die tolle Betreuung vor Ort und den unzähligen Überstunden, die für mich an der Apparatur, der Hilfe bei der Auswertung und den Korrekturen geleistet worden sind.
Christine Böhm für die nützliche Vorarbeit an der Laserionenquelle und für ihre Geduld mit meinen vielen Fragen und kleinen Bitten.
Kai Zuber für die spannenden und inspirierenden Privatvorlesungen über Neutrinos und den doppelten Betazerfall in der ISOLDE-Küche und im R1 und für die Hilfe beim Theorieabschnitt.
Der ganzen *ISOLTRAP-Collaboration* und im Besonderen den Leuten, die bei ISOLTRAP vor Ort und im Labor waren und immer mit vielen Anregungen, Diskussionen, moralischer Unterstützung und Hilfe die Arbeit und die Zeit an ISOLTRAP so spannend gemacht haben. Diese wären im einzelnen *Christopher Borgmann, Martin Breitenfeldt, Alexander Herlert, David Lunney, Sarah Naimi, Hiroshi Nakano, Dennis Neidherr, Kristian Petrik, Marco Rosenbusch, Lutz Schweikhard, Juliane Stanja und Robert Wolf.*
Kim Kreim und *Bruce Marsh*, auf deren wertvolles Expertenwissen zu Lasern und Laseroptik ich immer bauen konnte.
Ermano Barbero und dem *Werkstattteam von ISOLDE* für die Unterstützung bei den vielen kleinen Modifikationen der Quelle.
Dem *Werkstattteam* des Max Planck Instituts für Kernphysik in Heidelberg für die vielen Spezialanfertigungen.
Allen *MATS-Mitgliedern* und insbesondere hier *Martin Eibach, Jens Ketelaer, Szilard Nagy* und *Christian Smorra* vom TRIGA-TRAP Experiment für die Hilfe und den vielen Ideen zu der Laserionenquelle.
Der *Johannes Gutenberg-Universität Mainz*,dem *MPIK Heidelberg* und hier speziell *Sigrid Schipper*, *Gertraud Dücker* und *Tobias Emmerich.*
Der ganzen *Mainz Crew* für die verrückte Zeit in Mainz. Unter all den tollen Leuten noch einmal persönlich einen Dank an *Christoph Scherer* und *Alex Winkler*, die mir mindestenes eine komplette Physikbibliothek erspart haben und an *Christoph Seiffert* für die geteilten kleineren und mittleren Katastrophen im Studium.
Last but not least, denen, die von ganz Anfang an mit dabei waren und mich immer unterstützt haben, ganz egal von wo der Wind gerade wehte: Meine Eltern *Judith* und *Burghard* sowie meine Schwester *Bigna* und *Helga Thomas.*